Insight into the OH polarimetric structure of OH 26.5+0.6

S. Etoka[1][*], P. Diamond[1]

[1]*Jodrell Bank Centre for Astrophysics, School of Physics and Astronomy, The University of Manchester, Manchester M13 9PL, UK*

16 April 2010

ABSTRACT

We present the first view of the magnetic field structure in the OH shell of the extreme OH/IR star OH 26.5+0.6. MERLIN interferometric observations of this object were obtained in December 1993 in full polarisation, at 1612, 1665 and 1667 MHz. The maser spots show a spheroidal distribution both at 1612 and 1667 MHz, while at 1665 MHz emission from the blue-shifted maser peak is concentrated on the stellar position, and the red-shifted peak emission exhibits a filamentary structure oriented on a SE-NW axis. The linear polarisation in both main lines is rather faint, ranging from 9 to 20% at 1665 MHz and from 0 to 30% at 1667 MHz. At 1612 MHz most maser spots exhibit a similar range of linear polarisation although those in the outermost parts of the envelope reach values as high as 66%. This is particularly apparent in the southern part of the shell. The detailed distribution of the polarisation vectors could only be obtained at 1612 MHz. The polarisation vectors show a highly structured distribution indicative of a poloidal magnetic field inclined by 40-60° to the line of sight. The velocity distribution of the maser spots with respect to the radial distance is well explained by an isotropic outflow at constant velocity in the case of a prolate shaped spheroid envelope, also tilted about 45-65° to the line of sight.

Key words: polarisation - magnetic fields - stars: AGB and post-AGB - masers - circumstellar shell - stars:individual: OH 26.5+0.6

1 INTRODUCTION

After leaving the main sequence, low and intermediate mass stars experience a crucial phase in their evolution toward the white dwarf stage: the Asymptotic Giant Branch (AGB) phase. It is at the very end of this phase that the star will shed most of its mass through extensive mass loss (up to a few $10^{-4} M_\odot \mathrm{yr}^{-1}$). The exact evolutionary sequence along the AGB to this final stage has not yet been resolved, but OH/IR stars are thought to trace the period before the proto-planetary nebula stage. At that point, the central star is completely obscured in the optical by a thick dust shell built up by mass loss, but the envelope structure can be observed through strong emission in the ground state OH maser lines and at infrared wavelengths.

While AGB stars are fairly spherical objects, asymmetries such as elliptical shapes or bipolar outflows are commonly observed at the planetary nebula stage (Corradi & Schwarz 1995).

Recently, a series of papers investigated the polarimetric structure in the intermediate and outermost parts of the circumstellar shells of evolved stars (Bains et al. 2003, Etoka & Diamond 2004, Vlemmings et al. 2005, Vlemmings

& Diamond 2006). Although the origin and evolution of the magnetic field is not well understood and is currently a matter of debate, (cf. Nordhaus et al. 2007 and reference within), this series of papers has shown the importance of the magnetic field in shaping the circumstellar material.

OH 26.5+0.6 (AFGL 2205; IRAS 18348−0526) is an extreme OH/IR star at a distance of 1.37±0.30 kpc (van Langevelde et al. 1990). Its current mass-loss rate has been estimated to be on the order of 5×10^{-4} $M_\odot \mathrm{yr}^{-1}$ (Justtanont et al. 1996). It has been classified as a Very-Long Period Variable OH/IR star with a period of 1570 days (le Bertre 1993). Prior to that work, OH 26.5+0.6 has been imaged several times with the VLA at 1612 MHz with increasing sensitivity (Baud 1981; Bowers et al. 1983; Herman et al. 1985 and Bowers & Johnston 1990) where a complete ring-like structure is seen at virtually all velocities. It has also been imaged with MERLIN (Diamond et al. 1985), where the clumpiness of the shell was clearly revealed.

The work presented here is part II of a series of papers intending to unravel the magnetic structure around extreme OH/IR stars through observations in the ground state OH maser lines at 18 cm. The first paper of the series, Etoka & Diamond (2004, hereafter paper I), presents the magnetic field structure of the red supergiant NML Cyg at 1612 and

* E-mail: Sandra.Etoka@googlemail.com

1667 MHz. This first work has shown that a structured polarisation distribution exists for both lines linked with the geometry of the shell itself. This can be explained if the principal driver for the shaping of the shell is the magnetic field.

The details of the observations and data reduction process are given in Section 2. An analysis of the data is presented in Section 3. In Section 4 discussion and interpretation of the results is given, while conclusions are drawn in Section 5.

2 OBSERVATIONS & DATA REDUCTION

The observations were performed on the 12th December 1993 at 1612, 1665 and 1667 MHz using the 8 telescopes of MER-LIN available at that time (namely Defford, Cambridge, Knockin, Wardle, Darnhall, MK2, Lovell & Tabley) giving a maximum baseline of 217 km and a resolution of 0.17 arcsec. The observations lasted 12 hours from which three hours were spent on calibrator sources. Data were taken in full polarisation mode in order to retrieve the four Stokes parameters. A bandwith of 0.5 MHz was recorded and divided into 512 channels at correlation, leading to a channel separation of 1 kHz, giving a velocity resolution of 0.18 km s^{-1}. The observing programme switched at intervals of a few minutes between the three maser lines. The continuum source 3C84 was used to derive corrections for instrumental gain variations across the bandpass. 3C286 was also observed in order to retrieve the absolute polarisation position angles and to provide the flux density reference. The data reduction followed the procedure explained in paper I, section 2.2. All the velocities given in this article are relative to the local standard of rest (LSR).

3 ANALYSIS

3.1 MERLIN spectra

Andersson et al. (1974) originally discovered the intense OH maser signal at 18 cm emitted by OH 26.5+0.6. This Type II OH/IR supergiant has a maximum intensity observed in the 1612 MHz satellite line which is about 50 times greater than that in the 1665/1667 MHz mainlines.

The 1612 MHz spectrum of OH 26.5+0.6 in Stokes I, constructed from the final image, is shown in Fig.1. The spectral profile and the peak intensity ratio between the red- and the blue-shifted peaks of $I_{\rm red}/I_{\rm blue}$=2 has not changed since the detection of the source in 1973 by Andersson et al. (1974). The intensity and the profile retrieved from the final map show that we recovered most of the signal. A faint inter-peak emission can be observed in the spectrum presented by Andersson et al. in the velocity range [17-22] km s^{-1} and [33-35] km s^{-1}, not picked up by MERLIN. But the general agreement in the profile and peak flux intensity between the two sets of data indicates that the fraction of emission potentially lost in extended structures is minimal.
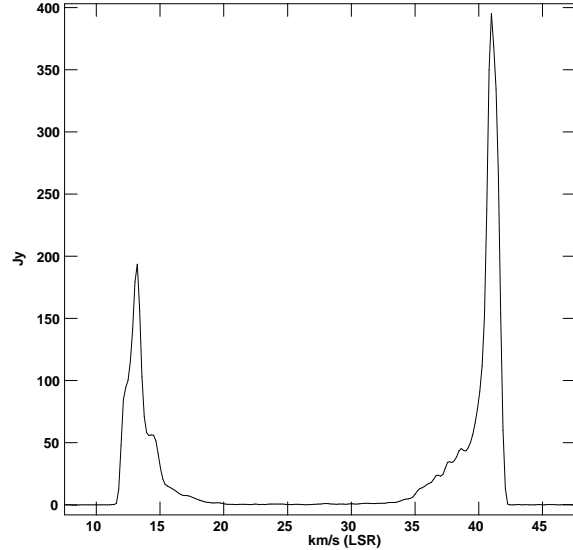
Figure 1. 1612 MHz spectrum of OH 26.5+0.6 in Stokes I constructed from the final image.

The spectra in Stokes I, constructed from the final image at 1667 and 1665 MHz, are shown in Figs. 2 and 3 respectively. The profile and the peak intensity ratio between the red- and the blue-shifted peaks $I_{\rm red}/I_{\rm blue} \simeq 0.5$ has not changed for the two mainlines since they were first detected. Nevertheless, we observed a stronger intensity corresponding to an increase of 40% at 1665 MHz and 30% at 1667 MHz from that recorded by Andersson et al. (1974) twenty years earlier, likely due to variability of the presumed unsaturated maser emission. This assumption is strengthened by single-dish observations presented by Etoka & Le Squeren (2004) taken with the Nançay radio telescope only three months after these MERLIN observations. With a periodicity of nearly 1600 days this corresponds to a phase difference of just 6%. The spectrum profile observed at 1667 MHz by MERLIN is entirely consistent with the single-dish observation. The spectrum observed at 1665 MHz with the Nançay radio telescope suggests faint inter-peak emission which is not picked up by MERLIN that could be the signature of faint extended emission. But, the peak flux in both mainlines is higher in the MERLIN spectra than in the single-dish observations (by about 10% at 1667 MHz and 35% at 1665 MHz). Such behaviour would be expected if both sets of observations were taken after the OH maximum, the steeper decrease of the 1665 MHz emission implying less saturated emission than that at 1667 MHz.

3.2 Maser emission extent and spot distributions

CLEANed maps of all the channels were created using the AIPS task IMAGR with a restoring beam of 0.342× 0.283 arcsec^2 at 1612 MHz and 0.350× 0.140 arcsec^2 at 1665 and 1667 MHz. The typical rms in Stokes I images, calculated over areas free of emission was about 8 mJy beam^{-1} increasing by up to 10 times that value for the channels with the strongest intensity.

The AIPS task SAD was used to identify maser components in the individual channel maps, as explained in pa-
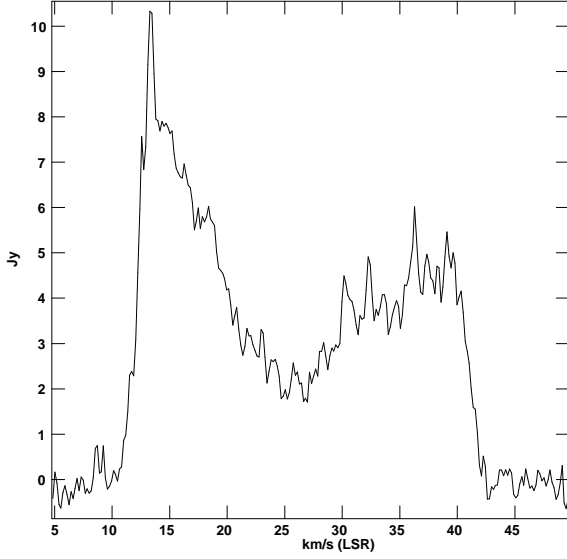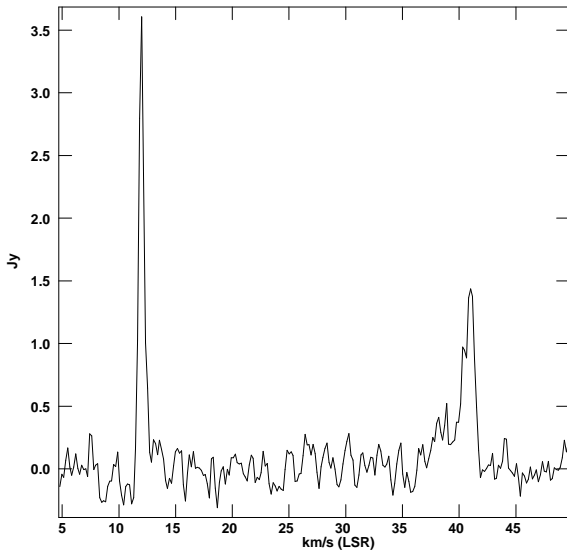
Figure 2. Same as Fig 1 at 1667 MHz.

Figure 3. Same as Fig 1 at 1665 MHz.

Figure 4. 1612 MHz velocity-integrated image of OH 26.5+0.6 in Stokes *I*. The contour levels shown are 1, 2, 4, 6, 8 and 10 times 0.40 Jy/Beam. In this velocity-integrated image the strong blue and red-peak contributions (corresponding to the velocity range [11:14] km s^{-1} and [37:42] km s^{-1}) have been cut off for dynamic range purposes.

maser spot number. The maser spots have been numbered in a decreasing velocity order. Column 2 gives the peak LSR velocity of the maser spot. Columns 3 to 6 present the corresponding I, Q, U and V flux densities. Column 7 presents the associated linear polarisation flux density. Columns 8 and 9 give the RA and DEC offsets from the pointing position. Columns 10 to 12 give the percentage of circular, linear and total polarisation, and finally column 13 gives the angle of the polarisation vector associated with the maser spot when relevant (i.e., for P$\geq 3\sigma$).

The strong difference between the number of maser spots found at 1612 and 1667 MHz (ratio of 4:1) is partly due to the 4σ cutoff. This eliminated more maser spots at 1667 MHz than it did at 1612 MHz because most of the components at 1667 MHz are faint and did not meet the criterion for 3 consecutive channels. This has an impact upon the inferred total extent of the shell at 1667 MHz, where the maser spot distribution modelling (cf. section 3.4) points to a substantially smaller radius than that suggested by the velocity integrated image in Stokes *I*.

3.2.1 Maser emission extent

The velocity-integrated images for the 1612, 1667 and 1665 MHz maser emission are presented in Figs. 4, 5 and 6 respectively. In Fig. 4, the strong blue- and red-peak contributions (corresponding to the velocity range [11:14] km s^{-1} and [37:42] km s^{-1}) have been cut off for dynamic range purposes. The 1612 and 1667 MHz extents are about 5 arcsec which corresponds to a linear extent of $\sim$7000 AU at 1.37 kpc. At 1612 MHz, the bulk of the emission describes a ring centred about +0.5 arcsec in δ from the optical stellar position. The 1665 MHz central core emission lies within

per I, section 3.2.1. At 1665 MHz, the simplicity of the maps was such that a 3σ threshold was taken to retrieve the maser components. At 1612 and 1667 MHz, the maps being complex, a more stringent selection was applied for retrieving the components. A component has been accepted only if its flux density was greater than 4×rms noise of a given channel (or greater than 10×rms noise in very complex regions). Similarly to paper I, the components were then grouped into maser spots if they existed in more than three consecutive channels and with positional offsets of less than 100 mas. With the given selection criteria, 10 maser spots were identified at 1665 MHz, 81 at 1667 MHz and 277 at 1612 MHz.

Tables 1 to 3 present the flux densities in Stokes parameters and polarisation properties of the maser spots fitted at 1612, 1667 and 1665 MHz respectively. The meaning of the 13 columns of these tables is as follows: column 1 gives the
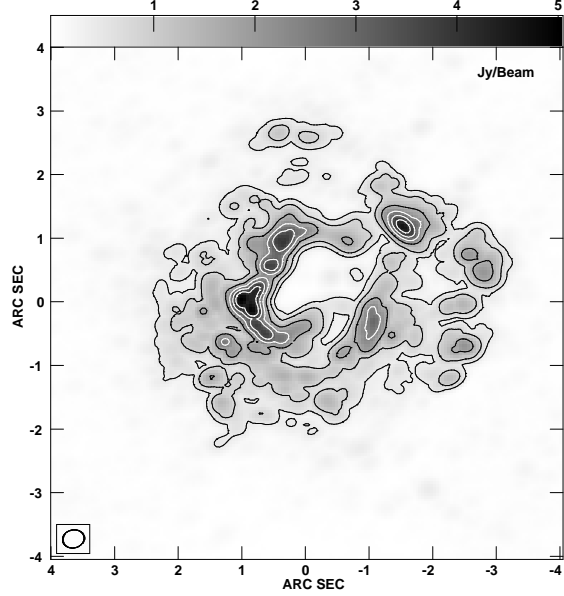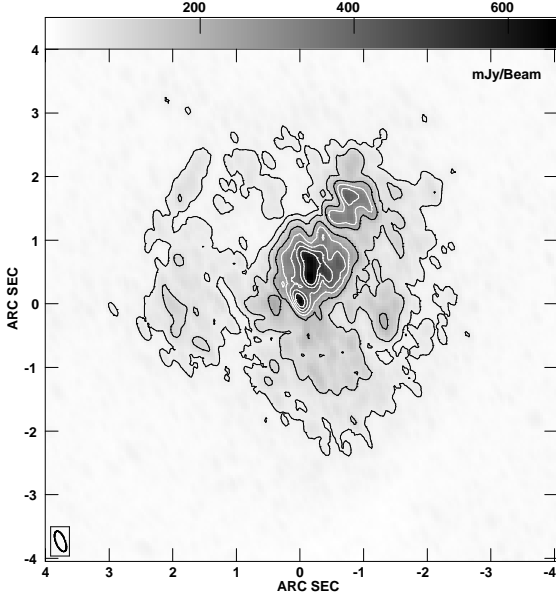
Figure 5. Same as Fig. 4 for 1667 MHz. The contour levels shown are 1, 2, 4, 6, 8, 10 and 12 times 0.044 Jy/Beam. This velocity-integrated image takes into account all the velocity channels in which emission was detected i.e., for the velocity range [11:42] km s^{-1}.
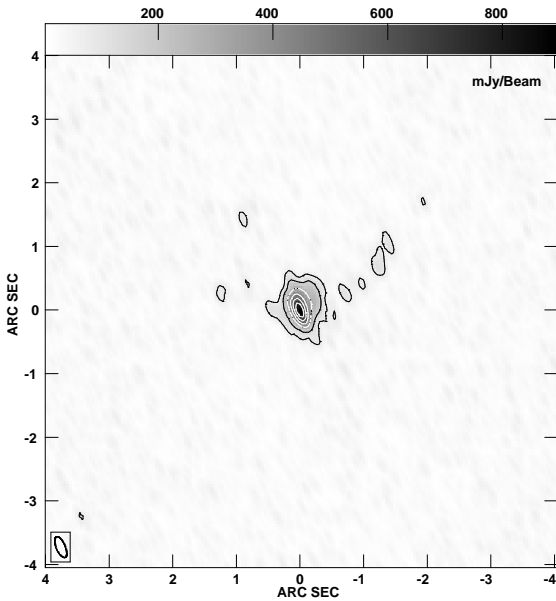
Figure 6. Same as Fig. 4 for 1665 MHz. The contour levels shown are 1, 2, 4, 6, 8 and 10 times 0.075 Jy/Beam. This velocity-integrated image takes into account all the velocity channels in which emission was detected i.e., for the velocity range [11.5:41.5] km s^{-1}.

an area less than 1.5 arcsec across. Including the very faint maser spots observed East and West, the total extent of the 1665-MHz emission is still less than 4 arcsec.

Figures 7 and 8 show the maps of the distribution of the emission integrated over a velocity interval of 1.27 and 1.23 km s^{-1} at 1612 and 1667 MHz respectively. From these

figures a certain number of physical properties concerning the geometry and the dynamic of the shell can be inferred:

• the ellipsoidal nature of the shell is revealed with an axis ratio of ~0.80 and a projected major axis position angle of $20° \pm 5°$. It is clearly apparent at 1612 MHz in the velocity range [23:18] km s^{-1}.

• at 1612 MHz, the maser emission distribution along the velocity channels is consistent with a radially expanding shell;

• at 1667 MHz, there is a hint of a deviation from the uniform radial expansion in the red-shifted emission since the 'central spot' expected at V=+41.7 km s^{-1} is not observed. Instead, a maser spot approximately 1 arcsec off-centre is observed;

• a clear asymmetry is observed, as an incomplete ring structure can be seen both at 1612 and 1667 MHz. At 1612 MHz, there is no detectable maser emission radiating from the north of the shell in the velocity range [33:20] km s^{-1}, while at 1667 MHz virtually no emission is observed in both the NW and SE quadrants in the same velocity range.

3.2.2 Location of the star

At the time of the observations, MERLIN data were not routinely phase-referenced. Therefore, an assumption regarding the location of the central star has to be made. As mentioned in paper I, amplification of the stellar radiation by the bluest emission of the spectrum has been observed for various types of OH/IR emitters, strongly suggesting that this feature marks the location of the star (Norris et al. 1984; Sivagnanam et al. 1990; van Langevelde et al. 2000). Therefore, the maser component belonging to the blue-shifted peak and located at the centre of the maser distributions at 1612 and 1667 MHz, at a velocity of 11.4 km s^{-1} and 12.2 km s^{-1} respectively (cf. Figs. 7 & 8) is quite likely to be over the stellar position. Similarly, the blue-shifted peak at V=12 km s^{-1} at 1665 MHz is taken to be centred at the stellar position.

This assumption has been followed for the analysis of the data presented in this article.

3.2.3 Maser spot distributions

Figures 9 to 11 present the maser spot distributions observed at 1612, 1667 and 1665 MHz respectively. The maser spots show a spheroidal distribution both at 1612 and 1667 MHz. But, 1612 MHz shows by far the most complex spatial velocity distribution, in which the outermost part of the distribution is dominated by blue-shifted maser spots.

At 1667 MHz, there is a rough gradient in the velocity distribution of the maser spots, such that the red-shifted spots are found in the N-NW part of the shell while the blue-shifted masers are found in the centre and S-SE part of the shell, contrasting with the 1612 MHz structure.

At 1665 MHz, emission from the blue peak is concentrated on the stellar position and the red-peak emission exhibits a filamentary structure oriented on a SE-NW axis.
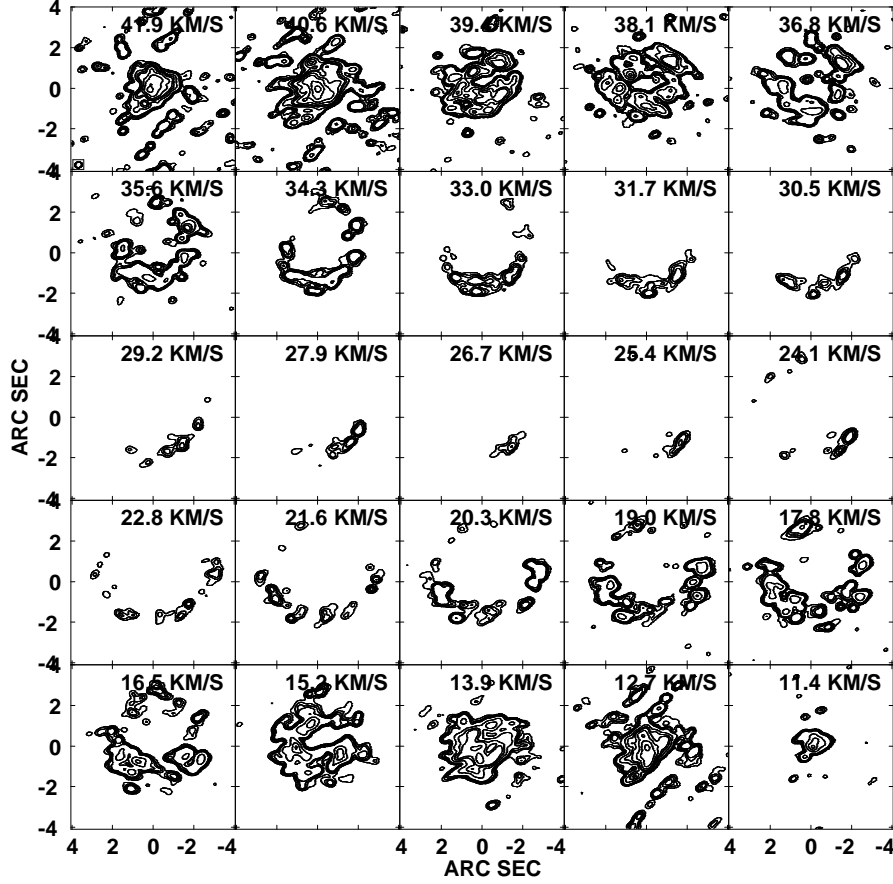
Figure 7. 1612 MHz maps of OH 26.5+0.6 in Stokes I. Each map is an integration of 7 channels (i.e., leading to a map separation of 1.27 km s^{-1}). The contour levels shown are 3, 4, 5, 7, 10, 30, 60, 90, 180, 360, 720 and 1440 times 0.019 Jy/Beam. The choice of the contours has been made so that the relatively faint emission can be seen in the velocity range [30-20] km s^{-1}. But this also stresses the dynamic range problem in channels where strong emission is present, that occurs around 41 km s^{-1} particularly but also around 12 km s^{-1} to a lesser extent.

3.3 Polarimetry

A few possible Zeeman patterns were found (cf. Fig. 12) leading to a magnetic field at the location of the OH shell $B = -3.7 \pm 0.3$ mG. At a similar distance, the magnetic field strength in NML Cyg has been estimated to be also about 3 mG (paper I).

The linear polarisation in both mainlines is rather faint, ranging from 9 to 20% at 1665 MHz and from 0 to 30% at 1667 MHz. At 1612 MHz, most maser spots exhibit a similar range but the outermost maser spots tend to exhibit a greater degree of linear polarisation, reaching values as high as 66%. The strongest linearly polarised components belong to the southern part of the shell.

The information concerning the magnetic field structure at the location of the OH maser emission is displayed in Figs. 9 to 11 via the vectors of polarisation which reveal the electric field plane at the polarised radiation. At 1667 MHz and 1665 MHz, only two maser spots had polarised flux P$\geq 3\sigma$. At 1612 MHz, out of the 277 maser spots detected, 106 had P$> 3\sigma$. Therefore the detailed polarisation vector distribution could only be obtained for the latter

transition. The vector distribution reveals a highly ordered polarisation field. Overall, the polarisation vectors show a mixture of radial and tangential distributions: the polarisation vectors in the N-NE part of the shell are radial while those in the S-SW are generally tangential. The position angle (PA) of the projected axis along which the tangential/radial separation occurs is about PA=100$° \pm 10°$. This is illustrated by Fig. 13 which presents a view on how the polarisation angles are related to the radial direction (PA$_c$) of their associated maser spot at 1612 MHz. More precisely, this figure shows the deviation of the vectors of polarisation from the tangent. The general trend observed clearly shows the change in direction of the polarisation vectors with orientation. A similar dichotomy in the orientation of the polarisation vector was observed by Boboltz (1997) for the Mira star R Aqr in SiO.

Goldreich et al. (1973) showed that in the limiting case of strong saturated maser emission and overlapping of the Zeeman components, a flip of 90$°$ in the plane of polarisation occurs when the angle between the magnetic field direction and the line of sight is close to the critical angle of $\sim$55$°$. Following Elitzur (1996) we can estimate the ratio χ_B for the significance of the Zeeman splitting:
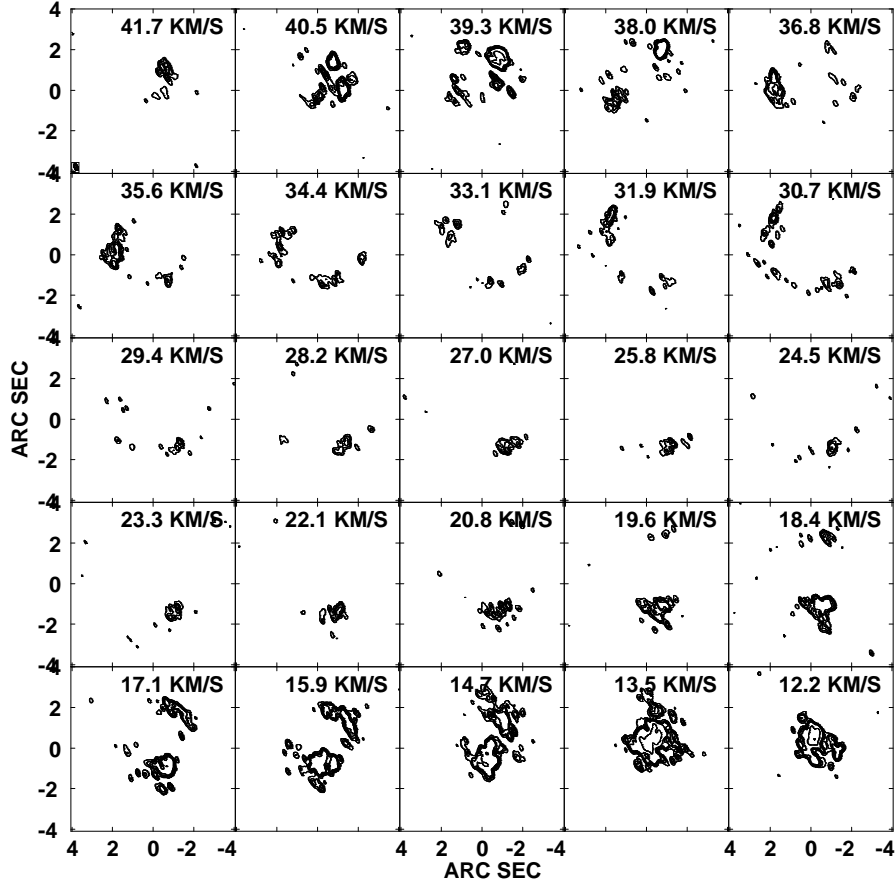
Figure 8. Same as Fig.7 for the 1667 MHz emission. The contour levels shown are 3, 4, 5, 7, 10 and 30 times 0.0042 Jy/Beam.
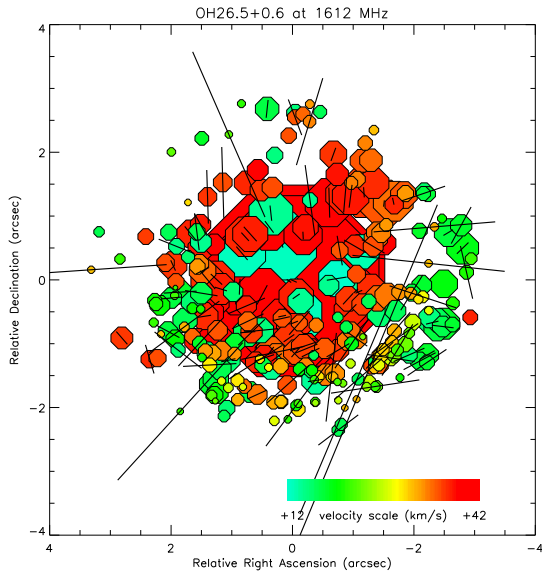
Figure 9. 1612 MHz maser spot distribution of OH 26.5+0.6. The area of a symbol is proportional to the maser spot intensity. The colour scale indicates velocity. Also plotted are the polarisation vectors associated with each maser spot with P> 3σ. The length of a vector is proportional to the percentage of linear polarisation.
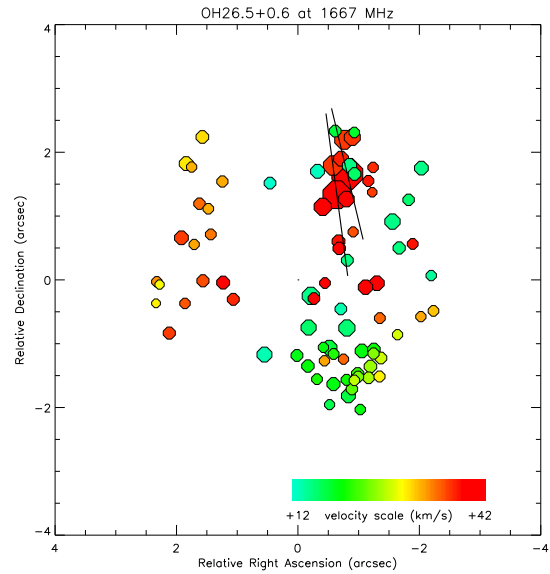
Figure 10. Same as Fig. 9 for the 1667 MHz.

$$\chi_B = \frac{\Delta\nu_B}{\Delta\nu_D} = 14g\lambda\frac{B}{\Delta v_D} \tag{1}$$

where the Lande factor g=0.935 for the $^2\Pi_{3/2}\, J\,=\,3/2$ (ground state) transitions of OH.
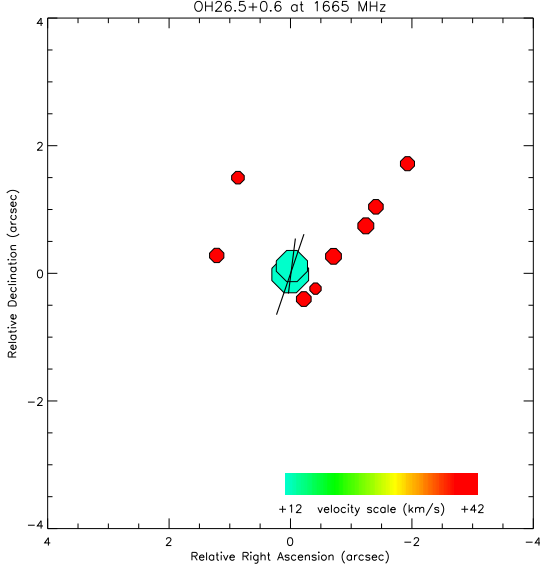
Figure 11. Same as Fig. 9 for the 1665 MHz.

For a magnetic field strength of 3.7 mG, $\chi_B = \frac{0.9}{\Delta v_D} < 1$ if $\Delta v_D > 0.9$ km s^{-1}, which has to be compared with the width of the line, found to be about 2 km s^{-1} (cf. Fig. 12). A magnetic field of the order of a few mG in the case of maser emission in the ground state of OH implies a Zeeman splitting exceeding the stimulated rate (i.e., g$\Omega >$ R). In addition, saturation of the 1612 MHz line implies a stimulated emission rate exceeding the decay constant (i.e, R$> \Gamma$). We therefore interpret the flip of the plane of linear polarisation observed in maser spots at 1612 MHz as due to the magnetic field being inclined by an angle close to $\theta_{crit} \sim 55°$ to the line of sight. Such a configuration accounts for the change of orientation of the polarisation vectors between tangential and radial as observed here. Such a flip in the polarisation angle has indeed already been observed in SiO and H$_2$O respectively (Kemball & Diamond 1997, Kemball et al. 2009 and Vlemmings & Diamond 2006). It has never been observed in OH so far though since usually the Zeeman pattern is fully separated.

3.4   Velocity distribution

The V=f(θ) distributions at 1612, 1667 and 1665 MHz are shown in Figs. 14(a,b,c), in which the maser component corresponding to the blue-shifted peak for all 3 lines has been taken to be at the stellar position (cf. Section 3.2.2) and the stellar velocity is taken to be V$_{star}$ = +27 km s^{-1} .

3.4.1   Comparison with the standard model

The simple model for a uniformly expanding spherical thin shell (Reid et al. 1977) is given by :

$$\left(\frac{\theta}{\theta_S}\right)^2 + \left(\frac{V - V_{star}}{V_{exp}}\right)^2 = 1 \qquad (2)$$

Where θ_S is the shell radius, V_{star} is the velocity of the star and V_{exp} the expansion velocity. Generally, this model

a)
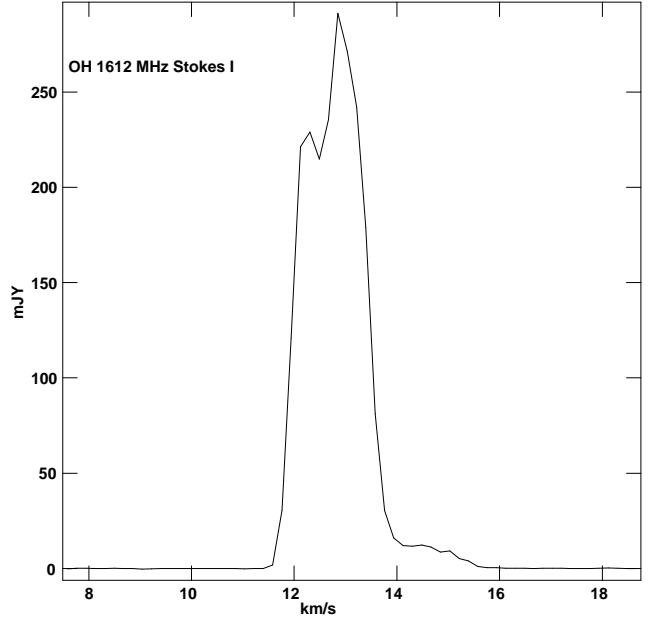
b)
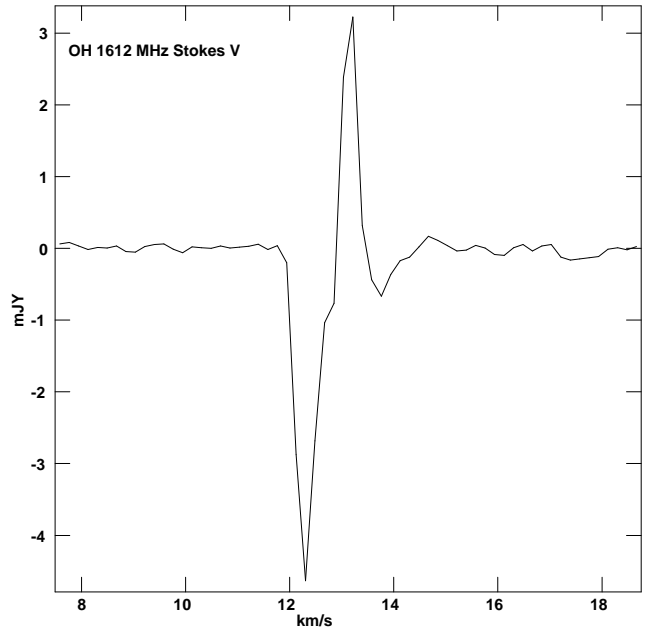
Figure 12. Stokes I and V spectrum for a Zeeman pair of a blue-shifted component at the relative position δRA=-90 mas and δDec=+180 mas. The separation between the 2 pairs provides an estimate of the magnetic field $B = -3.7\pm0.3$ mG that is pointing towards the observer.

provides a good explanation for the velocity distribution observed in OH/IR stars (Habing 1996). On the 3 figures are displayed the two best fits for the lower and upper boundaries of the radial velocity distribution. These are as follows:

• at 1612 MHz: $\theta_S = 1.4$ arcsec and $V_{exp} = 12$ km s^{-1} for the lower boundary (i.e., model 1 in Fig. 14a) and $\theta_S =$
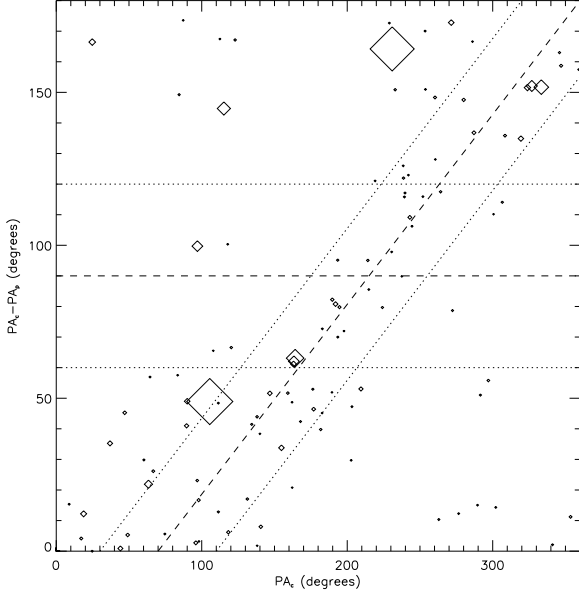
Figure 13. Difference in angle between the polarisation vector orientation and the radial direction (given by PA_c - PA_p) versus the position angle of the maser components (PA_c) at 1612 MHz. The size of the symbol is proportional to the corresponding maser spot intensity. The dashed line represents the best fit for the general trend observed. The dotted lines delineate a deviation of 20% from the best fit.

3.5 arcsec and V_{exp} = 15 km s^{-1} for the upper boundary (i.e., model 2 in Fig. 14a);

• at 1667 MHz: θ_S = 1.4 arcsec and V_{exp} = 12 km s^{-1} for the lower boundary (i.e., model 1 in Fig. 14b) and θ_S = 3.0 arcsec and V_{exp} = 18 km s^{-1} for the upper boundary (i.e., model 2 in Fig. 14b);

• at 1665 MHz: θ_S = 1.4 arcsec and V_{exp} = 12 km s^{-1} for the lower boundary (i.e., model 1 in Fig. 14c) and θ_S = 3.0 arcsec and V_{exp} = 16 km s^{-1} for the upper boundary (i.e., model 2 in Fig. 14c).

The simple model provides a reasonable explanation for the expansion of the inner shell. Also, it allows us to infer that the OH maser region has a certain thickness, which in the context of the standard model would be about 1.5-2 arcsec, and that acceleration is still taking place in the outer part of the circumstellar envelope. Both the 1612 and 1667 MHz distributions lead to similar results. But clearly, this model does not describe well the expansion of the outermost maser components. Indeed, the maximum shell radius is not observed at the stellar velocity, V_{star} = +27 km s^{-1}, but at two values equidistant from the stellar velocity, on either side of it. Sensitivity is not the cause since maser spots were indeed found around the stellar velocity range both at 1612 and 1667 MHz (cf. Table 1 and Table 2).

3.4.2   *Comparison with the models of Bowers (1991)*

Bowers (1991) produced a series of kinematic models as a tool to analyse complex aspherical outflows observed in the
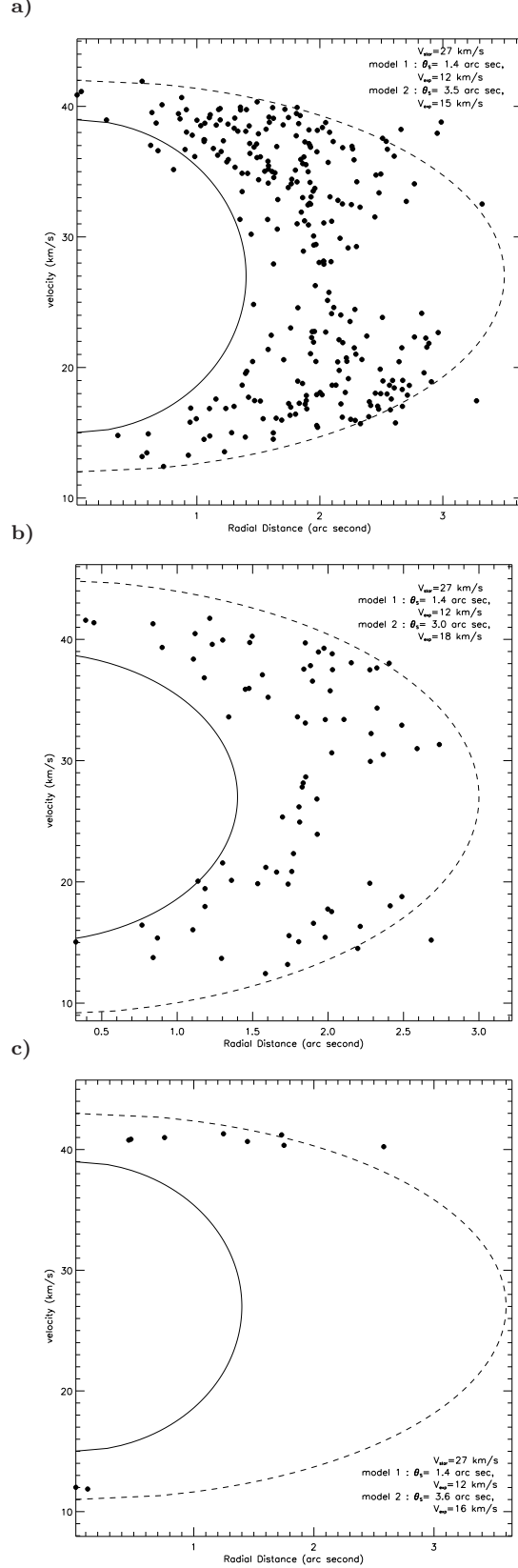
Figure 14. Velocity distribution of the maser spots versus the radial distance from the star projected on the plane of the sky at **a)** 1612 MHz, **b)** 1667 MHz and **c)** 1665 MHz. The inferred location of the star is RA=0 mas Dec=0 mas which is the location of the blue shifted peak in each line as explained Section 3.2.2.

cirmcumstellar shell of evolved stars. In these models, the maser emission is uniformly distributed throughout ellipsoidal shells with various orientations to the line of sight. The effect of rotation and radial acceleration that might be present in the velocity field is also taken into consideration. These models produce a large variety of possible $\theta(V)$ and $I(V)$ curves that may be applicable to stellar outflow. As an application of these models, the author successfully describes the shell structure of 3 different types of aspherical outflows commonly observed at the late stages of stellar evolution.

Overlaid on the 1612 MHz velocity distribution reproduced in Fig. 15, are two schematic models consistent with the distribution observed. The dotted line presents a schematic illustration of Bowers' model for an isotropic outflow at a constant velocity in the prolate case, where the inclination of the spheroid from the line of sight is $i = 45°$, while the continuous line is for the spheroid tilted from the line of sight by $i = 65°$. In the $i = 65°$ case, a standard double-peak spectral profile is expected while for $i = 45°$, for both the red and blue peaks, a double-component structure is expected, with the component closer to the stellar velocity being fainter than the external one. The intensity of the internal components increases when i decreases. There is indication of such an internal component structure in the 1612 MHz spectrum shown in Fig. 1. Consequently, both the $V=f(\theta)$ distribution and the spectral profile $I=f(V)$ are well explained by an isotropic outflow at constant velocity in the ellipsoidal prolate case, with an inclination to the line of sight between $45°$ and $65°$. Note that none of the other cases in the series of kinematic models presented by the Bowers are able to explain simultaneously the $V=f(\theta)$ and the spectral profile $I=f(V)$ we observe.

4 DISCUSSION

4.1 Actual stage of evolution of OH 26.5+0.6

The work of Sevenster (2002) and Ortiz et al. (2005) based on the MSX catalogue at the mid-infrared (MIR) wavelengths 8.3, 12.1, 14.7 and 21.3 μm showed that [8.3-14.7] vs [14.7-21.3] is better suited than the IRAS colour-colour diagram to separate AGB from post-AGB stars and that [15-21] vs [8-12] is the most efficient index to separate the four main classes of OH/IR objects: PPNs, SFRs, AGB and post-AGB stars. In the light of these results, we calculated the [8.3-12.1], [8.3-14.7] and [14.7-21.3] colour indices for OH 26.5+0.6 from the MSX measurement for this source to be 0.5669, 1.0832 and 0.0624 respectively. We then used these indices to locate OH 26.5+0.6 in the colour-colour diagrams of Ortiz et al. (2005) and Sevenster (2002).

Those values put OH 26.5+0.6 in the bluer OH/IR group of Ortiz et al. (2005), according to their classification based on the [8.3-14.7] and [14.7-21.3] indices. While it places it in the bulk of the AGB stars in Sevenster's (2002) diagram, based on the [14.7-21.3] and [8.23-12.13] colour-colour indices. This indicates that OH 26.5+0.6 is definitely still on the AGB at the present time.

Nevertheless, its IRAS [60-25] and [12-25] colour indices combined with its 18 cm OH maser properties attest to a thick circumstellar envelope characteristic of a
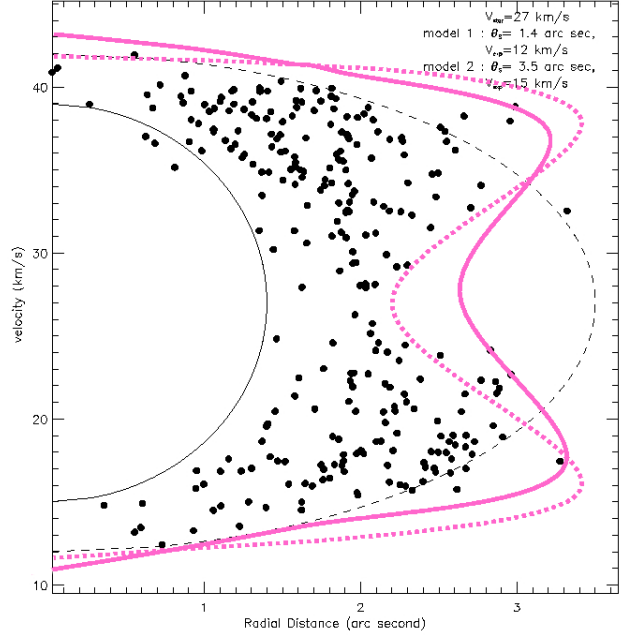
Figure 15. The radial velocity distributions at 1612 MHz on which is overlaid on top of the standard models (thin black lines), a series of schematic models in magenta illustrative of an isotropic outflow at a constant velocity in the prolate case, where the inclination of the spheroid from the line of sight is $i = 45°$ (thick dotted line) and $i = 65°$ (thick continuous line).

rather evolved AGB star (Etoka & Le Squeren 2004). Its infrared and OH characteristics resemble those observed for red OH/IR supergiants. It is one of the brightest OH maser emitters in our Galaxy, and in order to account for its infrared SED, Justtanont et al. (1996) evaluated its Main Sequence mass to be in the order of 8 $M_\odot$. The latter authors also estimated the current mass-loss rate of OH 26.5+0.6 to be on the order of 5×10^{-4} $M_\odot$/yr, triggered by the onset of a superwind phase just 150 years ago.

All this indicates that this object is at the tip of the AGB. This makes OH 26.5+0.6 a particular and important object in terms of stellar evolution: a junction object between an intermediate- and a high-mass evolved object on the verge of leaving the AGB towards the planetary nebula phase.

4.2 Distance considerations

The distance of OH 26.5+0.6 was calculated by van Langevelde et al. (1990) using phase lags which rely on the assumption of maser saturation, spherical symmetry and the thin shell model. The assumption of saturation for the OH 1612 MHz emission of Type II OH/IR has been demonstrated (Harvey et al. 1974, Etoka & Le Squeren 2000). Nonetheless it is clear from our results that the OH shell of OH 26.5+0.6 deviates from strictly spherical symmetry and the thin shell model condition. This deviation has consequently an impact on the actual distance inferred by van Langevelde et al. (1990). Indeed, as stated by those authors, phase lag measurement relies mainly on the reddest and bluest part of the spectral profile

while angular diameter determination from interferometric measurement relies on the velocity ranges closest to the stellar velocity. While the blue and red peaks, under the hypothesis of radial expansion, trace the front and rear caps of the shell along the line of sight, the velocity ranges responsible for the emission in the plane of the sky, that is in a perpendicular direction, are more internal. And the difference in depth is likely to be more important in the case of a thick shell. A direct consequence of the divergence from thin shell model, but still assuming spherical geometry, is the following:

$$\tau(D_{\mathrm{phase\,lag}}) \geq \tau(D_{\mathrm{int}}) \tag{3}$$

where $\tau(D_{\mathrm{phase\,lag}})$ is the time travel difference for emission coming from the front and rear caps of the shell separated by $D_{\mathrm{phase\,lag}}$ and, $\tau(D_{\mathrm{int}})$ is the time travel difference for emission coming from the total extent of the shell, D_{int}, as obtained from interferometric mapping (i.e., the time that would have been inferred if the observer was in the plane of the sky seeing the same object at an angle of $90°$). But because we are diverging from sphericity, with a prolate spheroid, this also implies that $D_{\mathrm{int}} > D_{\mathrm{phase\,lag}}$ which would have a compensating effect in this particular case. Herman et al. (1985) consider the impact of deviation from sphericity and the thin shell model on distance determination with phase lag. They conclude that an asymmetry of $\leq 20\%$ and the thickness of $\leq 20\%$ would set a limit of $\sim 10\%$ in the determination of the distance of OH/IR objects subject to these deviations. In our case, the more marked thickness of the shell would quite probably reduce the accuracy down to 20%. This shows the importance of better constraints on the actual shell properties (i.e., geometry and thickness) in order to get a more accurate distance determination from phase lag. Nonetheless, an uncertainty of 20%, already claimed by van Langevelde, would not have a major impact on the analysis presented here.

4.3 Faraday rotation

Faraday rotation could potentially rotate the polarisation vectors by a substantial angle if the radiation is propagating into an ionized medium. The change in the angle is given by:

$$\Delta\theta_{\mathrm{Faraday}} = \mathrm{RM}\lambda^2 \tag{4}$$

where RM is the rotation measure given by:

$$\mathrm{RM} = 0.812 \int_0^d [\frac{n_e(s)}{\mathrm{cm}^{-3}}][\frac{B(s)}{\mu G}](\frac{ds}{pc}) \tag{5}$$

(cf. Noutsos et al., 2008 their Equation 4).

The two main sources of Faraday rotation which could have an impact on the overall polarisation vectors are foreground rotation due to propagation in the interstellar medium (ISM) and, more importantly, rotation within the shell itself due to ionized material which would affect the linear polarisation of the red-shifted maser spots. We investigated these possible causes of Faraday rotation:

• Noutsos (private communication) calculated the RM at the location of OH 26.5+0.6 from adjacent pulsars to be RM ~ 7 rad m^{-2}. Such a value would produce a Faraday rotation of about $\Delta\theta_{\mathrm{Faraday}} = 13°$. Nonetheless, it has to be acknowledged that the uncertainty on this value is quite high due to the nature of the ISM and depends strongly on the density model adopted. In particular, adopting the electron density model (NE2001) of Cordes & Lazio (2002) would lead to a value of RM ~ 40 rad m^{-2} and potentially a rotation of $\Delta\Theta_{Faraday}$ of $\sim 74°$. But it also has to be noted that any general Faraday rotation occurring between the shell and the observer would not affect the general distribution observed, as it would rotate the overall polarisation vector angles by the same amount.

• Guilain & Mauron (1996) showed that for an Oxygen-rich AGB star a typical fractional electron abundance $x_e \sim 2\times10^{-5}$. Such a value would produce a maximum differential rotation of the polarisation vectors of $\sim 10°$. This would not change our fundamental results.

• Internal Faraday rotation from the denser central region itself is expected to be negligible since the size of the thin ionized hydrogen layer surrounding the central star has a typical thickness of less than 10^{12}cm. The overall region size is typically less than $2\mathrm{R}_{star}$ (i.e., <3 AU) to be compared with the typical maser spot size of at least 10-20 AU. This means that in the most pessimistic scenario it would affect at the very most 30% of the emission of those red-shifted maser spots on or very near the line of sight.

Consequently, we exclude Faraday rotation as a possible cause for the dichotomy observed in the polarisation angle distribution.

4.4 Shell structure and extent

At 1667 MHz, the emission in the south and the north-east of the shell extends beyond that at 1612 MHz by nearly 1 arcsec. This is an interesting result since mainline emission (i.e., 1665 and 1667 MHz) is expected to be internal to that of the 1612 MHz satellite line due to the difference in pumping schemes. The 1612 MHz transition is largely pumped by absorption at 35 and 53 μm radiation, whilst the mainlines are pumped by a radiative absorption from the ground state to $^2\Pi_{3/2} J = 5/2$, followed by a collisional de-excitation, which requires a high density than the 1612 MHz mechanism (Gray 2007). Competitive gain (Field 1985) can affect the balance of the intensities in the mainlines. Observing 1667 MHz emission beyond that of the 1612 MHz requires deviation from the standard model (Collison & Nedoluha 1995).

Fong et al. (2002) imaged the circumstellar envelope of OH 26.5+0.6 in the ^{12}CO $J = 1-0$ line. Their observations show a deconvolved source size of 8.8×5.5 arcsec^2. In order to account for the observed flux, they needed to include a second, more tenuous, AGB wind and conclude that up to 80% of the CO flux comes from the unresolved superwind.

Chesneau et al. (2005) observed OH 26.5+0.6 at 8.7 μm with the VLTI. Their deconvolved image exhibits asymmetry resulting in a elliptical shape with an axis ratio of 0.75 and a mean position angle (PA) of $95°\pm6°$. The authors

suggest that the flattened distribution observed in the mid-infrared could be explained by either an equatorial overdensity or a disk close to an edge-on configuration.

Both the ellipticity and the mean position angle inferred by the latter authors relating to material close to the star, are in agreement with our new findings but at the OH maser location.

All this observational evidence shows that divergence from spherical symmetry is already present and observable at different resolutions in the whole gaseous and dusty envelope of OH 26.5+0.6. This provides us with strong evidence that, in this case, the onset of asymmetry does indeed start as early as the late-AGB phase. The two-step mechanism proposed by Sahai (2002) in which a high-speed collimated outflow (in other words, an anisotropic superwind) would carve an imprint within an intrinsically spherical AGB mass-loss envelope could be in action.

4.5 Role of the magnetic field in the shaping process ?

From the magnetic field strength of 3.7 mG measured from Zeeman splitting (cf Section 3.3), we can infer the corresponding magnetic energy density ϵ_B at the location of the OH maser emission:

$$\epsilon_B = B^2/(2\mu_0) = \frac{10^{-1}}{8\pi} B_{\mathrm{Gauss}}^2 = 5.5 \times 10^{-8}\,\mathrm{J\,m^{-3}} \qquad (6)$$

And, we can compare it with the thermal and kinetic energy densities $\epsilon_{Thermal}$ and $\epsilon_{Kinetic}$ respectively. According to the model of Goldreich & Scoville (1976), at a distance $r \sim 10^{16}$cm, the number density of hydrogen in the wind of an OH/IR star is typically $n_H = 10^5$ cm^{-3} which is generally taken to be the typical distance for (mainline) OH maser emission. Nevertheless, we found that the maser extent at 1612 MHz attests to a radius of about 3500 AU, that is $r \sim 5.5 \simeq 10^{16}$ cm=875×R$_{star}$ in the model of Goldreich & Scoville, for which n_H drops to 10^4 cm^{-3}. Adopting nonetheless a conservative value of $n_H = 10^5$ cm^{-3}, and T=100 K, leads to the following for the thermal and kinetic densities:

$$\epsilon_{Thermal} = \frac{3}{2} n_H kT \sim 2 \times 10^{-10}\,\mathrm{J\,m^{-3}} \qquad (7)$$

and

$$\epsilon_{Kinetic} = \frac{1}{2}\rho V_{exp}^2 \sim 1.8 \times 10^{-8}\,\mathrm{J\,m^{-3}} \qquad (8)$$

with V_{exp}=15 km s^{-1}.

This indicates that the magnetic energy density dominates over the thermal energy density and is at least 3 times greater than the kinetic energy density.

Figure 16 presents, superimposed on top of the maser spot and polarisation vector distributions: 1) the ellipse that describes best the maser spot distribution observed; 2) the axis separating the radial and tangential vectors of polarisa-

tion, and 3) the direction of the magnetic field which would produce such a distribution of the vectors of polarisation.

As previously mentioned, the position angle determined by Chesneau et al. (2005) for the mid-infrared emission is in agreement with the semi-major axis orientation on the plane of the sky of the 1612 MHz ellipsoid distribution as observed here.

The axis separating the tangential and radial distribution of the polarisation vectors accounting for a magnetic field direction of 40-60° is aligned with the major axis of the geometrically ellipsoidal maser emission (cf. Fig. 16). This latter projected ellipse, and the velocity distribution of the maser spots as observed in Fig. 15 are indeed expected if the actual shell geometry is a prolate spheroid tilted about 45-65° to the line of sight (Bowers 1991). These combined results reveal that there is a definite correlation between the magnetic field orientation and the geometrical structure of the circumstellar envelope.

5 CONCLUSION

The infrared and 18 cm OH maser properties of OH 26.5+0.6 attest to a thick circumstellar envelope, characteristic of a rather evolved star most probably at the tip of the AGB. The 1612 MHz emission reveals an ellipsoidal geometry, while the presumably more central 1665 MHz emission traces a filamentary structure. Both 1612 and 1667 MHz high resolution maps show a lack of maser emission from some parts of the shell, and in the southern and north-eastern part of the shell, 1667 MHz emission extends beyond that at 1612 MHz. All these deviations from the standard spherical model show that the OH/IR stage (i.e., late-AGB phase) is clearly at the stage where asymmetry starts to develop. The presence of acceleration in the shell at the OH maser location may be a secondary factor enhancing the asymmetry observed so far away from the star. The root of this asymmetry is likely to be close to the stellar surface itself, as near infrared results indicate. This latter hypothesis is reinforced by the agreement in orientation of the major axis of the elliptic distribution observed in infrared and at 1612 MHz. Finally, we found that the magnetic field strength, inferred from OH Zeeman splitting, is such that the magnetic field energy density dominates over the thermal and kinetic pressures and that there is a definite correlation between the magnetic field orientation and the main axis of geometrically ellipsoidal maser emission. This suggests that the magnetic field plays a role in the shaping process observed.

a)

b)

Figure 16. a) Distribution of the maser spots at 1612 MHz as shown in Fig. 9, on which is overlaid a model explaining both the geometric and polarimetric structures observed. **b)** A 3D representation of the model in which the line of sight is perpendicular to the plane of the page.

with MERLIN, a National Facility operated by the University of Manchester at Jodrell Bank Observatory, on behalf of STFC.

REFERENCES

Andersson C., Johansson L.E.B., Goss W.M., Winnberg A., Nguyen-Quang-Rieu, 1974, A&A, 30, 475

Bains I., Gledhill T.M., Yates J.A., Richards, A.M.S., 2003, MNRAS, 338, 287

Baud B., 1981, ApJ, 250L, 79

Boboltz D.A., 1997, PhD

Bowers P.F., Johnston K.J., Spencer J.H., 1983, ApJ, 274, 733

Bowers P.F., Johnston K.J., 1990, ApJ, 354, 676

Bowers P.F., 1991, ApJS, 76, 1099

Chesneau O., Verhoelst T., Lopez B., Waters L.B.F.M., Leinert Ch., Jaffe W., Köhler R., de Koter A., Dijkstra C., 2005, A&A, 435, 563

Collison A.J., Nedoluha G.E., 1995, ApJ, 442, 311

Cordes J. M., Lazio T. J. W., 2002, astro.ph, 7156

Corradi R.L.M., Schwarz H.E., 1995, A&A, 293, 871

Diamond P.J., Norris R.P., Rowland P.R., Booth R.S., Nyman L-A., 1985, MNRAS, 212, 1

Elitzur M., 1996, ApJ, 457, 415

Etoka S., Le Squeren A.M., 2000, A&AS, 146, 179

Etoka S., Diamond P.J., 2004, MNRAS, 348, 34 (paper I)

Etoka S., Le Squeren A.M., 2004, A&A, 420, 217

Field D., 1985, MNRAS, 217, 1

Fong D., Justtanont K., Meixner M., Campbell M. T., 2002, A&A, 396, 581

Goldreich P., Keeley D. A., Kwan J. Y., 1973, ApJ, 179, 111

Goldreich P., Scoville N., 1976, ApJ, 205, 144

Gray M.D., 2007, MNRAS, 375, 477

Guilain C., Mauron N., 1996 A&A, 314, 585

Habing H., 1996, A&A Rev, 7, 97

Harvey P.M., Bechis K.P., Wilson W.J., Ball J.A., 1974, ApJS, 27, 331

Herman J., Baud B., Habing H.J., Winnberg A., 1985, A&A, 143, 122

Justtanont K., Skinner C.J., Tielens A.G.G.M., Meixner M., Baas F., 1996, ApJ, 456, 337

Kemball A.J., Diamond P.J., 1997, ApJ, 481, L111

Kemball A.J., Diamond P.J., Gonidakis I., Mitra M., Yim K., Pan K.-C., Chiang H.-F., 2009, ApJ, 698, 1721

Le Bertre T., 1993, A&AS, 97, 729

Nordhaus J., Blackman E.G., Frank A., 2007, MNRAS, 376, 599

Norris R.P., Booth, R.S., Diamond P.J., Nyman L.-A., Graham D. A., Matveenko L. I., 1984, MNRAS, 208, 435

Noutsos A., Johnston S., Kramer M., Karastergiou A., 2008, MNRAS, 386, 1881

Ortiz R., Lorenz-Martins S., Maciel W.J., Rangel E.M., 2005, A&A, 431, 565

Reid M.J., Muhleman D.O., Moran J.M., Johnston K.J., Schwartz P.R., 1977, ApJ, 214, 60

Sahai R., 2002, *Rev. Mex. Astron. Astrofis. Ser. Conf.* 13, 133

Sevenster M., 2002, AJ, 123, 2772

Sivagnanam P., Diamond P.J., Le Squeren A.M., Biraud F., 1990, A&A, 229, 171

van Langevelde H.J., van der Heiden R., van Schooneveld C., 1990, A&A, 239, 193

van Langevelde H.J., Vlemmings W., Diamond P. J., Baudry A., Beasley A.J., 2000, A&A, 357, 945

Vlemmings V.H.T., van Langevelde H.J., Diamond P.J., 2005, A&A, 434, 1029

Vlemmings V.H.T., Diamond P.J., 2006, ApJ 648L, 59

Table 1. Stokes parameter flux densities and polarisation properties of the 1612 MHz maser spots.

No	Vel (km s^{-1})	I (Jy b^{-1})	Q (Jy b^{-1})	U (Jy b^{-1})	V (Jy b^{-1})	P (Jy b^{-1})	$\Delta\alpha$ (milli arcsec)	$\Delta\delta$ (milli arcsec)	m_c (%)	m_l (%)	m_t (%)	χ (°)
1	41.921	4.829	0.088	-0.147	0.121	0.171	501.38	-236.10	2.5	3.5	4.3	-29.5
2	41.139	63.344	-0.236	0.551	-0.169	0.600	58.00	-16.10	-0.3	0.9	0.9	56.6
3	40.873	50.169	-0.394	0.416	-0.520	0.573	-19.88	-16.16	-1.0	1.1	1.5	66.7
4	40.676	5.481	0.138	-0.013	-0.340	0.139	869.41	-107.05	-6.2	2.5	6.7	-2.7
5	40.344	1.750	-0.004	-0.020	<-0.012	<0.020	1399.67	-510.60	<-0.7	<1.2	<1.4	/
6	40.123	2.518	0.030	0.003	0.023	0.030	-174.57	694.78	0.9	1.2	1.5	2.9
7	39.941	3.989	0.189	0.011	-0.043	0.189	-606.08	1210.50	-1.1	4.7	4.8	1.7
8	39.917	0.754	0.001	0.010	<-0.017	<0.010	572.82	1722.28	<-2.3	<1.3	<2.6	/
9	39.904	0.956	-0.010	0.006	<0.011	<0.012	-1509.47	577.15	<1.2	<1.2	<1.7	/
10	39.834	2.142	-0.211	-0.086	-0.076	0.228	323.63	-1144.03	-3.5	10.6	11.2	-78.9
11	39.776	1.035	-0.004	0.006	<-0.005	<0.007	1414.57	-970.78	<-0.5	<0.7	<0.9	/
12	39.758	1.307	-0.027	-0.032	0.107	0.042	-298.22	-1138.00	8.2	3.2	8.8	-65.1
13	39.751	0.752	0.003	0.011	-0.048	<0.011	1288.79	554.21	-6.4	<1.5	<6.6	/
14	39.749	3.777	0.020	0.084	-0.032	0.086	382.58	830.36	-0.8	2.3	2.4	38.3
15	39.724	1.822	-0.006	-0.005	-0.100	0.008	1311.45	-341.11	-5.5	0.4	5.5	-70.1
16	39.526	2.611	-0.070	-0.031	0.040	0.077	184.59	-606.88	1.5	2.9	3.3	-78.1
17	39.452	0.857	0.009	0.012	<-0.006	<0.015	-736.63	1652.95	<-0.7	<1.8	<1.9	/
18	39.436	1.113	0.015	0.003	<-0.010	<0.015	-214.94	822.43	<-0.9	<1.4	<1.7	/
19	39.361	3.226	-0.029	-0.028	0.067	0.040	-1092.81	-185.92	2.1	1.2	2.4	-68.0
20	39.290	1.055	-0.006	0.003	-0.026	<0.007	1571.21	-957.57	-2.5	<0.6	<2.6	/
21	39.174	1.158	0.003	0.013	<-0.007	<0.013	1507.58	493.04	<-0.6	<1.2	<1.3	/
22	39.143	0.713	0.014	0.025	<0.008	0.029	1514.56	866.10	<1.1	4.0	<4.1	30.4
23	39.138	1.584	-0.046	-0.042	-0.160	0.062	-228.67	-1077.14	-10.1	3.9	10.8	-68.8
24	39.099	1.090	-0.030	-0.021	-0.044	0.037	464.77	-1222.62	-4.0	3.4	5.2	-72.5
25	39.081	2.295	0.080	-0.022	-0.024	0.083	-957.08	1310.33	-1.0	3.6	3.7	-7.7
26	39.039	0.695	-0.033	-0.032	<0.015	0.046	759.84	-408.79	<2.2	6.6	<7.0	-67.9
27	38.962	1.652	-0.030	0.019	-0.218	0.036	1180.73	-142.93	-13.2	2.1	13.4	73.8
28	38.955	2.049	-0.011	-0.026	<-0.007	0.028	-61.84	-257.47	<-0.3	1.4	<1.4	-56.5
29	38.935	2.121	0.004	0.065	-0.075	0.065	696.02	718.59	-3.5	3.1	4.7	43.2
30	38.798	0.374	-0.006	-0.015	<0.004	<0.016	-2928.66	-587.08	<1.1	<4.3	<4.4	/
31	38.778	2.605	0.141	-0.026	0.035	0.143	-868.11	1331.31	1.3	5.5	5.7	-5.2
32	38.761	0.581	-0.002	0.014	-0.057	<0.014	-1674.73	1176.87	-9.8	<2.4	<10.1	/
33	38.722	2.241	-0.020	-0.017	<-0.014	0.026	-33.80	-667.74	<-0.6	1.2	<1.3	-69.8
34	38.707	1.738	-0.002	-0.051	0.099	0.051	-948.46	-482.63	5.7	2.9	6.4	-46.1
35	38.680	1.286	0.006	0.038	-0.025	0.038	1677.90	723.81	-1.9	3.0	3.6	40.5
36	38.643	2.271	-0.007	0.056	-0.138	0.056	1252.56	9.05	-6.1	2.5	6.6	48.6
37	38.585	0.965	0.013	-0.004	<0.010	<0.014	763.84	1520.21	<1.0	<1.4	<1.7	/
38	38.567	0.873	-0.019	0.030	-0.025	0.036	-1031.10	525.45	-2.9	4.1	5.0	61.2
39	38.518	2.684	0.002	0.048	-0.092	0.048	780.08	675.60	-3.4	1.8	3.8	43.8
40	38.504	0.717	-0.034	-0.064	<0.008	0.072	607.02	-1289.27	<1.1	10.1	<10.2	-59.0
41	38.380	1.609	0.010	-0.009	<0.017	<0.013	-1336.37	1515.50	<1.1	<0.8	<1.4	/
42	38.322	1.337	0.020	-0.009	0.060	<0.022	-1296.84	-129.09	4.5	<1.6	<4.8	/
43	38.249	1.310	-0.029	-0.009	-0.269	0.030	1454.36	-571.17	-20.5	2.3	20.6	-81.4
44	38.230	0.522	0.020	0.014	<-0.008	0.024	2351.69	-1242.69	<-1.5	4.7	<4.9	17.5
45	38.196	0.585	0.049	0.003	<-0.012	0.049	1399.17	1301.85	<-2.1	8.4	<8.7	1.8
46	38.159	1.310	0.015	0.019	-0.027	0.024	1966.54	225.95	-2.1	1.8	2.8	25.9
47	38.102	0.803	-0.018	-0.029	<-0.019	0.034	-748.65	-1102.81	<-2.4	4.3	<4.9	-60.9
48	38.088	1.932	0.010	0.072	-0.044	0.073	1397.50	-0.30	-2.3	3.8	4.4	41.0
49	38.020	1.426	-0.012	-0.028	<-0.003	0.030	58.18	-913.48	<-0.2	2.1	<2.1	-56.6
50	38.012	1.223	0.020	-0.018	-0.029	0.027	-673.31	1966.92	-2.4	2.2	3.3	-21.0
51	37.940	0.825	0.002	0.022	-0.027	<0.022	2810.69	-909.99	-3.3	<2.7	<4.3	/
52	37.899	0.816	0.020	0.004	<-0.022	<0.020	518.78	1407.60	<-2.7	<2.5	<3.7	/
53	37.793	1.043	0.001	-0.025	-0.024	0.025	-915.31	-296.99	-2.3	2.4	3.3	-43.9
54	37.745	4.373	0.070	0.011	0.148	0.071	-1176.85	1372.36	3.4	1.6	3.8	4.5
55	37.557	0.426	0.010	-0.004	<0.001	<0.011	2416.70	678.23	<0.2	<2.5	<2.5	/
56	37.450	0.983	-0.037	-0.026	<-0.008	0.045	-178.83	-1042.53	<-0.8	4.6	<4.7	-72.5
57	37.435	0.783	-0.004	-0.047	-0.049	0.047	674.24	-820.53	-6.3	6.0	8.7	-47.4
58	37.363	0.776	-0.002	-0.012	<0.001	<0.012	-1152.55	-385.19	<0.1	1<.6	<1.6	/
59	37.323	0.509	-0.001	-0.007	<-0.007	<0.007	2223.57	-1226.21	<-1.4	<1.4	<2.0	/
60	37.305	0.544	-0.010	-0.004	0.076	<0.011	-1054.65	90.31	14.0	<2.0	<14.1	/
61	37.305	0.527	-0.003	-0.017	<0.005	<0.017	2091.19	268.01	<0.9	<3.3	<3.4	/
62	37.278	0.454	-0.005	-0.011	-0.031	<0.012	-1306.93	-1348.28	<-6.8	<2.7	<7.3	/
63	37.154	0.684	-0.015	0.025	-0.109	0.029	-1329.35	524.84	-15.9	4.3	16.5	60.5
64	37.145	0.603	0.067	0.004	0.037	0.067	1148.67	1527.21	6.1	11.1	12.7	1.7

Table 1. *continued*

No	Vel (km s^{-1})	I (Jy b^{-1})	Q (Jy b^{-1})	U (Jy b^{-1})	V (Jy b^{-1})	P (Jy b^{-1})	$\Delta\alpha$ (milli arcsec)	$\Delta\delta$ (milli arcsec)	m_c (%)	m_l (%)	m_t (%)	χ ($^\circ$)
65	37.119	0.723	0.009	0.008	<-0.004	<0.012	331.27	1447.99	<-0.6	<1.7	<1.8	/
66	37.012	0.552	-0.002	-0.016	-0.031	<0.016	170.30	-600.27	-5.6	<2.9	<6.3	/
67	37.002	0.446	-0.001	0.000	-0.040	<0.001	1919.21	-28.14	-9.0	<0.2	<9.0	/
68	36.936	0.411	0.005	0.004	<-0.006	< 0.006	62.48	2260.37	<-1.5	<1.6	<2.2	/
69	36.920	0.580	-0.008	-0.050	-0.038	0.051	88.38	-1646.85	-6.6	8.7	10.9	-49.5
70	36.880	0.657	-0.006	-0.009	-0.040	<0.011	1233.32	-790.36	-6.1	<1.6	<6.3	/
71	36.871	3.750	0.038	-0.010	0.044	0.039	-1506.80	1196.46	1.2	1.0	1.6	-7.4
72	36.837	0.896	0.015	-0.008	<-0.012	<0.017	-1137.62	1865.76	<-1.3	<1.9	<2.3	/
73	36.774	1.035	0.002	-0.022	<-0.013	<0.022	-54.59	-1132.63	<-1.3	<2.1	<2.5	/
74	36.737	1.229	0.009	0.004	-0.054	<0.010	-1835.57	1329.67	-4.4	< 0.8	<4.5	/
75	36.713	0.388	0.017	0.016	<0.003	0.023	-41.52	2548.44	<0.8	6.0	<6.1	21.6
76	36.694	0.477	0.021	0.008	<0.019	<0.022	-778.12	459.82	<4.0	<4.7	<6.2	/
77	36.604	0.441	0.002	-0.022	<-0.020	<0.022	-113.12	-674.22	<-4.5	<5.0	<6.7	/
78	36.540	0.710	-0.010	-0.018	-0.024	<0.021	-530.65	-1073.55	-3.4	<2.9	<4.5	/
79	36.521	0.433	0.010	-0.005	<-0.002	<0.011	-1446.48	-1346.15	<-0.5	<2.6	<2.6	/
80	36.396	1.114	-0.009	-0.008	<-0.002	<0.012	-1401.29	-290.51	<-0.2	<1.1	<1.1	/
81	36.259	1.408	0.005	-0.022	-0.039	0.023	357.55	-1112.85	-2.8	1.6	3.2	-38.6
82	36.182	0.346	-0.008	0.007	<0.006	<0.011	-172.89	2598.76	<1.7	<3.1	<3.5	/
83	36.155	0.613	-0.023	-0.026	<0.008	0.035	737.49	-649.11	<1.3	5.7	<5.8	-65.7
84	36.137	0.934	0.011	0.015	-0.092	<0.019	-1371.87	646.00	-9.9	<2.0	<10.1	/
85	36.130	0.424	-0.007	0.003	<0.008	<0.008	1647.20	-885.42	<1.9	<1.8	<2.6	/
86	36.075	1.218	-0.019	-0.023	<-0.010	0.030	1481.46	143.95	<-0.8	2.4	<2.5	-64.8
87	35.937	0.353	-0.004	-0.002	<-0.002	<0.004	792.32	-1665.77	<-0.6	<1.3	<1.4	/
88	35.920	0.495	-0.010	-0.019	<0.005	<0.021	-973.64	-792.60	<1.0	<4.3	<4.4	/
89	35.905	0.872	0.014	0.011	<0.007	<0.018	-1292.59	1875.62	<0.8	<2.0	<2.2	/
90	35.796	0.745	0.009	-0.005	-0.071	<0.010	-1390.81	745.06	-9.5	<1.4	<9.6	/
91	35.747	1.322	-0.009	-0.026	<-0.011	0.028	261.10	-1215.68	<-0.8	2.1	<2.2	-54.5
92	35.706	2.730	0.028	0.013	0.061	0.031	-1659.93	1232.14	2.2	1.1	2.5	12.5
93	35.613	0.411	-0.002	-0.025	<-0.009	0.025	-1436.42	-1182.28	<-2.2	6.1	<6.5	-47.3
94	35.535	0.664	-0.016	-0.017	<0.010	0.023	580.18	-1795.53	<1.5	3.5	<3.8	-66.6
95	35.450	1.068	-0.004	-0.005	<-0.004	<0.006	-1562.65	-247.15	<-0.4	<0.6	<0.7	/
96	35.339	0.679	-0.014	-0.007	-0.024	<0.016	-904.16	-948.06	-3.5	<2.3	<4.2	/
97	35.189	0.793	-0.002	-0.010	-0.046	<0.010	-542.70	-1485.43	-5.8	<1.3	<5.9	/
98	35.159	0.349	0.002	0.004	<-0.006	<0.004	-391.33	-709.66	<-1.7	<1.3	<2.1	/
99	35.113	0.292	0.017	0.005	<-0.012	<0.018	-966.51	1519.74	<-4.1	<6.1	<7.3	/
100	35.027	0.565	-0.009	-0.011	<0.022	<0.014	1529.96	257.08	<3.9	<2.5	<4.6	/
101	35.007	0.626	0.009	0.005	<0.015	<0.010	1168.03	-1110.50	<2.4	<1.6	<2.9	/
102	34.993	0.437	0.009	0.006	<-0.022	<0.011	-1067.96	1576.80	<-5.0	<2.5	<5.6	/
103	34.907	0.608	-0.008	0.013	-0.023	<0.015	-1461.51	732.37	-3.8	<2.5	<4.5	/
104	34.869	0.449	-0.010	-0.012	<-0.017	<0.016	-216.38	-1349.83	<-3.8	<3.5	<5.2	/
105	34.862	0.645	-0.010	0.024	<-0.006	0.026	-1065.42	-927.17	<-0.9	4.0	<4.1	56.3
106	34.811	0.266	0.031	-0.022	<-0.010	0.038	-281.75	2479.64	<-3.8	14.3	<14.8	-17.7
107	34.739	0.359	0.005	-0.014	<-0.005	<0.015	-1197.96	2144.34	<-1.4	<4.1	<4.3	/
108	34.545	0.649	0.005	-0.020	<0.006	<0.021	-696.72	-1468.22	<0.9	<3.2	<3.3	/
109	34.415	0.404	0.011	0.018	0.039	<0.021	-1761.31	-188.84	9.7	<5.2	<11.0	/
110	34.378	0.304	0.011	-0.007	<0.005	<0.013	954.45	-1159.32	<1.6	<4.3	<4.6	/
111	34.223	0.449	0.010	0.019	<0.008	<0.021	-1860.68	1352.62	<1.8	<4.8	<5.1	/
112	34.215	0.332	-0.018	-0.004	<0.007	<0.018	1434.12	-1111.03	<2.1	<5.6	<6.0	/
113	34.177	0.318	-0.010	-0.019	<0.001	<0.021	188.17	-1910.46	<0.3	<6.8	<6.8	/
114	34.120	0.410	0.003	0.009	<-0.003	<0.009	1566.01	208.99	<-0.7	<2.3	<2.4	/
115	34.067	0.291	0.011	0.009	<0.007	<0.014	-1544.23	859.50	<2.4	<4.9	<5.5	/
116	34.067	0.133	0.016	-0.003	<0.003	<0.016	-285.79	2753.86	<2.3	<12.2	<12.4	/
117	33.778	0.445	-0.010	-0.007	<-0.015	<0.012	1311.37	-1147.63	<-3.4	<2.7	<4.3	/
118	33.720	0.250	0.013	-0.008	<-0.022	<0.015	-1947.73	-210.36	<-8.8	<6.1	<10.7	/
119	33.505	0.305	-0.010	-0.013	<-0.021	<0.016	313.43	-1919.98	<-6.9	<5.4	<8.8	/
120	33.471	0.401	0.007	-0.012	<-0.004	<0.014	195.47	-1353.84	<-1.0	<3.5	<3.6	/
121	33.373	0.126	-0.025	-0.004	<0.013	0.025	-2337.64	830.66	<10.3	20.1	<22.6	-85.5
122	33.074	0.262	0.018	0.004	<-0.001	<0.018	901.37	-1877.17	<-0.4	<7.0	<7.0	/
123	33.065	0.166	-0.008	-0.022	<-0.012	0.023	1781.81	-736.69	<-7.2	14.1	<15.8	-55.0
124	33.012	0.337	0.003	-0.026	<-0.019	0.026	-1678.90	-799.77	<-5.6	7.8	<9.6	-41.7
125	32.860	0.158	-0.008	-0.005	<0.004	<0.009	-669.28	-1516.65	<2.5	<6.0	<6.5	/
126	32.801	0.084	0.038	-0.041	<0.003	0.056	-1055.22	-1869.69	<3.6	66.5	<66.6	-23.6
127	32.722	0.156	-0.014	0.010	<-0.005	<0.017	-1341.07	2346.78	<-3.2	<11.0	<11.5	/
128	32.573	0.260	-0.005	-0.016	<-0.019	<0.017	188.56	-1907.28	<-7.3	<6.4	<9.7	/

Table 1. *continued*

No	Vel (km s⁻¹)	I (Jy b⁻¹)	Q (Jy b⁻¹)	U (Jy b⁻¹)	V (Jy b⁻¹)	P (Jy b⁻¹)	$\Delta\alpha$ (milli arcsec)	$\Delta\delta$ (milli arcsec)	m_c (%)	m_l (%)	m_t (%)	χ (°)
129	32.526	0.074	0.018	-0.020	<0.006	0.027	-862.02	-2005.87	<8.1	36.4	<37.3	-24.0
130	32.519	0.093	-0.023	-0.003	<0.007	0.023	3315.37	159.03	<7.5	24.9	<26.0	-86.3
131	32.507	0.241	-0.013	-0.005	<-0.016	<0.014	-1346.97	-1375.27	<-6.6	<5.8	<8.8	/
132	32.474	0.101	-0.025	0.005	<0.008	0.025	-2241.52	258.98	<7.9	25.2	<26.4	84.3
133	32.447	0.271	-0.011	-0.026	<-0.011	0.028	-1636.80	-970.94	<-4.1	10.4	<11.2	-56.5
134	32.276	0.085	0.010	-0.006	<-0.010	<0.012	2165.88	-849.78	<-11.8	<13.7	<18.1	/
135	31.899	0.256	0.004	-0.021	-0.052	<0.021	-1491.64	-1092.73	-20.3	<8.4	<22.0	/
136	31.591	0.075	0.003	0.006	<0.005	<0.007	1721.89	1213.72	<6.7	<8.9	<11.1	/
137	31.341	0.146	0.013	-0.013	<0.013	<0.018	535.95	-1239.13	<8.9	<12.6	<15.4	/
138	31.332	0.239	-0.005	-0.012	<0.008	<0.013	-423.54	-1516.96	<3.3	<5.4	<6.3	/
139	31.230	0.393	-0.011	-0.008	<-0.017	<0.014	-1463.49	-1172.58	<-4.3	<3.5	<5.5	/
140	31.197	0.148	0.005	-0.006	<-0.013	<0.008	-2073.78	-303.81	<-8.8	<5.3	<10.3	/
141	31.071	0.330	-0.003	-0.010	<0.019	<0.010	-93.69	-2029.81	<5.8	<3.2	<6.6	/
142	31.008	0.290	0.011	-0.011	<0.005	<0.016	906.37	-1572.29	<1.7	<5.4	<5.7	/
143	30.921	0.341	-0.030	-0.003	0.023	0.030	1363.14	-1333.78	6.7	8.8	11.1	-87.1
144	30.596	0.177	0.024	-0.006	<0.006	0.025	-638.42	-1525.51	<3.4	14.0	<14.4	-7.0
145	30.464	0.113	0.003	-0.008	<0.019	<0.009	393.04	-1371.29	<16.8	<7.6	<18.4	/
146	30.065	0.314	0.004	-0.007	<-0.004	<0.008	-1603.82	-1107.58	<-1.3	<2.6	<2.9	/
147	29.892	0.243	-0.023	0.016	<-0.010	0.028	-2147.57	-265.41	<-4.1	11.5	<12.2	72.6
148	29.422	0.119	0.002	-0.005	< 0.008	<0.005	1167.59	-1584.84	<6.7	<4.5	<8.1	/
149	29.369	0.240	0.008	0.012	<-0.005	<0.014	-1422.82	-1334.40	<-2.1	<6.0	<6.4	/
150	29.258	0.126	0.002	0.008	<-0.012	<0.008	-2246.46	-480.60	<-9.5	<6.5	<11.5	/
151	29.151	0.157	-0.008	-0.005	<-0.012	<0.009	298.68	-2209.26	<-7.6	<6.0	<9.7	/
152	28.905	0.094	0.003	-0.019	<-0.003	<0.019	817.08	-1677.35	<-3.2	<20.5	<20.7	/
153	28.138	0.423	-0.032	0.009	<0.010	0.033	-1621.02	-1223.50	<2.4	7.9	<8.3	82.1
154	28.127	0.235	-0.004	-0.010	<0.002	<0.011	-1268.36	-1584.09	<0.9	<4.6	<4.7	/
155	28.099	0.437	0.011	0.011	-0.024	<0.016	-1982.93	-663.28	-5.5	<3.6	<6.6	/
156	28.036	0.160	0.006	0.002	<0.006	< 0.006	1056.14	-1691.25	<3.8	<4.0	<5.5	/
157	27.925	0.146	-0.006	-0.007	<0.011	<0.009	-956.74	-1311.27	<7.5	<6.3	<9.8	/
158	27.905	0.092	-0.004	-0.012	<-0.004	<0.013	-754.40	-1887.18	<-4.3	<13.7	<14.4	/
159	26.272	0.084	0.010	-0.016	<-0.008	<0.019	-376.40	-1926.35	<-9.5	<22.5	<24.4	/
160	25.750	0.141	-0.004	-0.006	<0.008	<0.007	-1221.28	-1675.94	<5.7	<5.1	<7.6	/
161	25.139	0.297	-0.002	-0.006	<-0.003	<0.006	-1678.68	-1197.86	<-1.0	<2.1	<2.3	/
162	24.829	0.066	0.006	-0.005	<0.015	<0.008	-1157.18	-891.49	<22.7	<11.8	<25.6	/
163	24.589	0.408	-0.016	-0.013	<-0.014	<0.021	-1857.41	-1007.41	<-3.4	<5.1	<6.1	/
164	24.571	0.102	0.004	0.002	<0.009	<0.004	-831.13	-1620.59	<8.8	<4.4	<9.8	/
165	24.442	0.062	0.009	-0.020	<-0.012	<0.022	1271.81	-1897.95	<-19.4	<35.4	<40.4	/
166	24.150	0.125	0.004	0.019	<-0.014	<0.019	1994.61	2004.59	<-11.2	<15.5	<19.1	/
167	24.124	0.198	0.002	0.013	<-0.004	<0.013	-1923.11	-831.54	<-2.0	<6.6	<6.9	/
168	24.019	0.245	0.010	-0.011	<-0.005	<0.015	-1384.83	-1670.73	<-2.0	<6.1	<6.4	/
169	23.835	0.097	0.018	0.021	<-0.011	0.028	1048.40	2278.84	<-11.3	28.5	<30.7	24.7
170	23.524	0.184	0.013	0.003	<0.006	<0.013	1330.09	-1809.05	<3.3	<7.3	<8.0	/
171	23.030	0.095	0.013	-0.017	<-0.003	<0.021	-740.42	-1599.07	<-3.2	<22.5	<22.7	/
172	22.763	0.116	-0.010	-0.012	<0.011	<0.016	1941.04	-243.95	<9.5	<13.5	<16.5	/
173	22.747	0.115	0.002	-0.004	<0.015	<0.004	-93.70	-1935.23	<13.0	<3.9	1<3.6	/
174	22.709	0.245	0.010	-0.021	-0.023	0.023	-1727.83	-1098.38	-9.4	9.5	13.4	-32.3
175	22.672	0.239	-0.010	-0.010	0.023	<0.014	-2943.53	331.37	9.6	<5.9	<11.3	/
176	22.471	0.121	0.002	0.002	<0.007	<0.003	-358.74	-1564.01	<5.8	<2.3	<6.2	/
177	22.400	0.145	-0.007	-0.003	-0.029	<0.008	2285.83	-667.93	-20.0	<5.3	<20.7	/
178	22.328	0.074	0.001	-0.022	<0.022	<0.022	1849.37	-2061.00	<29.7	<29.8	<42.1	/
179	22.286	0.040	-0.002	-0.002	<-0.012	<0.003	1929.18	-122.15	<-30.0	<7.1	<30.8	/
180	22.248	0.185	0.010	-0.007	<-0.010	<0.012	2842.62	326.88	<-5.4	<6.6	<8.5	/
181	22.121	0.170	-0.024	-0.007	<-0.016	0.025	-1361.61	-1671.20	<-9.4	14.7	<17.4	-81.9
182	21.942	0.151	-0.001	-0.011	<-0.017	<0.011	-374.94	-1912.30	<-11.3	<7.3	<13.5	/
183	21.901	0.101	-0.010	-0.019	<-0.008	<0.021	76.45	-2184.84	<-7.9	<21.3	<22.7	/
184	21.847	0.111	0.005	0.010	<-0.006	<0.011	840.73	2761.49	<-5.4	<10.1	<11.5	/
185	21.555	0.330	0.025	0.013	<0.011	0.028	-2867.32	118.45	<3.3	8.5	<9.1	13.7
186	21.504	0.286	-0.015	-0.013	0.037	0.020	-2640.83	-367.48	12.9	6.9	14.6	-69.5
187	21.498	0.309	-0.014	-0.007	<0.005	<0.016	2248.24	-377.63	<1.6	<5.1	<5.3	/
188	21.377	0.119	-0.005	-0.013	<0.010	<0.014	1511.46	-457.19	<8.4	<11.7	<14.4	/
189	21.051	0.128	0.009	-0.003	<-0.009	<0.009	1490.96	-1215.88	<-7.0	<7.4	<10.2	/
190	21.016	0.339	-0.003	-0.003	<-0.003	<0.004	2269.72	-321.95	<-0.9	<1.3	<1.6	/
191	20.732	0.499	-0.011	-0.014	<0.020	<0.018	1286.10	-1803.97	<4.0	<3.6	<5.4	/
192	20.612	0.109	0.000	-0.005	<0.002	<0.005	-1770.70	-1532.36	<1.8	<4.6	<4.9	/

Table 1. *continued*

No	Vel (km s^{-1})	I (Jy b^{-1})	Q (Jy b^{-1})	U (Jy b^{-1})	V (Jy b^{-1})	P (Jy b^{-1})	$\Delta\alpha$ (milli arcsec)	$\Delta\delta$ (milli arcsec)	m_c (%)	m_l (%)	m_t (%)	χ (°)
193	20.595	0.208	-0.009	0.005	<-0.003	<0.010	1647.09	-444.01	<-1.4	<4.9	<5.1	/
194	20.470	0.670	0.005	0.004	<-0.004	<0.006	2183.36	-398.83	<-0.6	<1.0	<1.2	/
195	20.458	0.203	0.008	-0.032	0.025	0.033	-61.33	-1966.64	12.3	16.2	20.3	-38.0
196	20.456	0.222	0.001	-0.004	<0.004	<0.004	-321.62	-1416.98	<1.8	<1.9	<2.6	/
197	20.440	0.138	0.000	-0.004	<-0.018	<0.004	-2462.98	961.17	<-13.0	<2.9	<13.3	/
198	20.424	0.575	0.006	-0.005	< 0.022	<0.008	1933.90	-927.86	<3.8	<1.4	<4.0	/
199	19.868	1.308	0.005	-0.013	-0.082	<0.014	-2489.87	-61.88	-6.3	<1.1	<6.4	/
200	19.773	0.754	-0.014	-0.011	-0.028	<0.018	1232.07	-1770.65	-3.7	<2.4	<4.4	/
201	19.708	0.292	-0.002	-0.011	<0.007	< 0.011	-120.90	-1399.99	<2.4	<3.8	<4.5	/
202	19.594	1.750	-0.004	-0.046	-0.072	0.046	-2803.13	497.16	-4.1	2.6	4.9	-47.5
203	19.548	0.325	0.010	-0.029	<0.013	0.031	-972.46	-1000.92	<4.0	9.4	<10.2	-35.5
204	19.140	0.394	-0.010	-0.008	<-0.007	<0.013	-2095.09	768.95	<-1.8	<3.3	<3.8	/
205	19.005	0.323	-0.007	-0.004	<-0.011	<0.008	1493.92	2217.22	<-3.4	<2.5	<4.2	/
206	19.000	1.653	-0.010	0.009	-0.176	0.013	-2498.62	-686.71	-10.6	0.8	10.6	69.0
207	18.976	0.340	0.001	-0.034	<-0.011	0.034	1530.95	-991.75	<-3.2	10.0	<10.5	-44.2
208	18.964	0.887	-0.013	-0.021	-0.190	0.025	-2220.02	-1177.25	-21.4	2.8	21.6	-60.9
209	18.907	0.779	0.026	-0.044	-0.065	0.051	-2778.28	855.26	-8.3	6.6	10.6	-29.7
210	18.774	0.980	-0.053	-0.006	-0.046	0.053	1848.80	-192.05	-4.7	5.4	7.2	-86.8
211	18.649	0.667	0.004	-0.010	-0.036	<0.011	-2129.14	-82.04	-5.4	<1.6	<5.6	/
212	18.646	0.646	-0.006	-0.006	<-0.015	<0.008	944.55	-989.66	<-2.3	<1.3	<2.6	/
213	18.640	1.159	-0.011	-0.009	<-0.005	<0.014	1318.96	-1633.61	<-0.4	<1.2	<1.3	/
214	18.635	0.379	-0.012	-0.026	-0.150	0.029	-2215.78	-1294.05	-39.6	7.6	40.3	-57.4
215	18.627	0.373	0.004	0.009	-0.074	<0.010	-2636.20	-699.91	-19.8	<2.6	<20.0	/
216	18.437	0.387	0.001	0.002	<-0.004	<0.002	-2231.28	1344.35	<-1.0	<0.6	<1.2	/
217	18.313	1.326	-0.012	-0.020	<-0.008	0.023	-2565.01	740.75	<-0.6	1.8	<1.9	-60.5
218	18.090	0.635	-0.016	0.022	-0.044	0.027	2054.21	-806.03	-6.9	4.3	8.1	63.0
219	18.086	1.115	-0.019	0.011	<0.004	<0.022	1262.53	-1553.57	<0.4	<2.0	<2.0	/
220	18.028	0.568	-0.020	-0.027	-0.107	0.034	-2093.88	-1273.90	-18.8	5.9	19.7	-63.3
221	17.993	1.152	-0.011	0.018	-0.034	<0.021	-2378.00	-753.58	-3.0	<1.8	<3.5	/
222	17.966	0.342	-0.021	-0.015	<-0.017	0.026	-2156.48	1353.26	<-5.0	7.5	<9.0	-72.2
223	17.916	0.498	0.013	-0.030	-0.029	0.033	-1963.99	-199.81	-5.8	6.6	8.8	-33.3
224	17.907	0.728	-0.023	-0.004	<-0.013	0.023	1998.20	-284.12	<-1.8	3.2	<3.7	-85.1
225	17.873	0.948	0.026	-0.006	<0.020	0.027	417.77	2679.38	<2.1	2.8	<3.5	-6.5
226	17.846	0.737	0.004	-0.011	-0.025	<0.012	695.85	-1757.36	-3.4	<1.6	<3.8	/
227	17.718	0.464	-0.009	0.001	<0.021	<0.009	485.34	-1334.25	<4.5	<2.0	<4.9	/
228	17.587	0.738	-0.026	0.006	<0.003	0.027	-2475.18	-730.73	<0.4	3.6	<3.6	83.5
229	17.581	0.265	0.001	-0.008	<-0.004	<0.008	-886.49	-740.05	<-1.5	<3.0	<3.4	/
230	17.466	0.419	-0.003	-0.009	<0.007	<0.009	-1381.09	-1289.53	<1.7	<2.3	<2.9	/
231	17.463	0.261	0.001	-0.014	<0.003	<0.014	-298.33	-1438.59	<1.1	<5.4	<5.5	/
232	17.447	0.188	-0.008	-0.008	<-0.019	<0.011	3186.43	752.88	<-10.1	<6.0	<11.7	/
233	17.426	0.792	-0.041	0.013	-0.042	0.043	1501.73	-208.09	-5.3	5.4	7.6	81.2
234	17.381	0.255	-0.016	-0.004	<-0.005	<0.016	-803.08	-2264.06	<-2.0	<6.5	<6.8	/
235	17.258	0.862	-0.013	-0.006	-0.059	<0.014	1195.05	-1388.75	-6.8	<1.7	<7.0	/
236	17.238	0.463	0.026	0.007	<-0.021	0.027	1575.27	752.84	<-4.5	5.8	<7.3	7.5
237	17.209	0.440	-0.003	0.017	<-0.010	<0.017	2038.68	746.90	<-2.3	<3.9	<4.5	/
238	17.193	1.020	-0.015	-0.003	<-0.020	<0.015	1769.77	-634.81	<-2.0	<1.5	<2.5	/
239	17.092	0.239	-0.007	-0.017	<0.006	<0.018	1127.44	-2133.95	<2.5	<7.7	<8.1	/
240	17.036	0.272	-0.007	-0.021	<-0.003	<0.022	-754.32	-2352.03	<-1.1	<8.1	<8.2	/
241	17.020	0.357	0.008	-0.008	<-0.008	<0.011	-1258.30	-335.07	<-2.2	<3.2	<3.9	/
242	17.020	0.289	0.011	0.012	<-0.007	<0.016	-456.22	2632.04	<-2.4	<5.6	<6.1	/
243	16.960	0.742	-0.005	-0.008	-0.024	<0.009	-1695.47	-484.01	-3.2	<1.3	<3.5	/
244	16.882	0.189	-0.005	-0.003	<-0.003	<0.006	-747.02	-586.42	<-1.6	<3.1	<3.5	/
245	16.852	1.406	-0.035	-0.005	-0.059	0.035	737.08	-819.55	-4.2	2.5	4.9	-85.9
246	16.825	0.251	-0.005	-0.025	-0.023	0.025	-1081.93	-1554.08	-9.2	10.2	13.7	-50.7
247	16.807	0.166	-0.011	-0.007	<0.005	<0.013	-349.15	-1182.91	<3.0	<7.9	<8.5	/
248	16.802	0.947	-0.001	0.016	<0.012	<0.016	-2395.34	-634.11	<1.3	<1.7	<2.1	/
249	16.752	0.527	0.002	-0.014	<0.022	<0.014	-2170.51	1382.92	<4.2	<2.7	<5.0	/
250	16.423	0.739	-0.008	0.006	<-0.012	<0.010	1400.29	-1134.44	<-1.6	<1.4	<2.1	/
251	16.337	0.290	-0.006	0.012	<-0.014	<0.013	1720.36	359.42	<-4.8	<4.6	<6.6	/
252	16.229	1.194	-0.023	-0.011	<-0.007	0.025	-2302.23	-670.04	<-0.6	2.1	<2.2	-77.2
253	16.128	0.348	-0.010	0.032	<-0.009	0.034	1884.80	-1100.48	<-2.6	9.6	<9.9	53.7
254	16.113	0.966	-0.021	-0.009	-0.064	0.023	1057.26	-1259.56	-6.6	2.4	7.0	-78.4
255	16.076	1.174	-0.006	-0.011	<-0.013	<0.013	-1445.23	-527.52	<-1.1	<1.1	<1.6	/
256	16.074	0.652	0.005	0.008	-0.035	<0.009	977.27	-187.73	-5.4	<1.4	<5.6	/

Table 1. *continued*

No	Vel (km s^{-1})	I (Jy b^{-1})	Q (Jy b^{-1})	U (Jy b^{-1})	V (Jy b^{-1})	P (Jy b^{-1})	$\Delta\alpha$ (milli arcsec)	$\Delta\delta$ (milli arcsec)	m_c (%)	m_l (%)	m_t (%)	χ (°)
257	16.029	0.466	-0.018	-0.018	<0.006	0.025	-1919.01	-1176.00	<1.3	5.5	<5.7	-67.5
258	15.968	0.799	-0.009	0.010	-0.039	<0.013	1652.97	-350.53	-4.9	<1.7	<5.2	/
259	15.948	0.450	-0.019	-0.004	-0.041	<0.019	1082.06	-2015.52	-9.1	<4.3	<10.1	/
260	15.805	1.069	-0.060	-0.011	0.027	0.061	516.80	-790.25	2.5	5.7	6.2	-84.8
261	15.751	0.514	0.015	0.006	0.028	<0.016	-46.10	2614.48	5.4	<3.1	<6.2	/
262	15.685	0.770	-0.009	-0.006	<-0.019	<0.011	-2255.16	-584.81	<-2.5	<1.4	<2.9	/
263	15.548	0.451	0.007	0.005	<0.003	<0.009	292.72	1952.60	<0.7	<1.9	<2.0	/
264	15.411	0.426	-0.020	0.018	<-0.010	0.027	1910.47	525.17	<-2.3	6.3	<6.7	69.0
265	15.006	0.376	0.040	0.012	<-0.005	0.042	-288.46	1249.65	<-1.3	11.1	<11.2	8.3
266	14.993	0.746	0.010	0.018	<0.017	<0.021	1508.17	595.07	<2.3	<2.8	<3.6	/
267	14.917	0.697	-0.010	-0.009	<0.010	<0.013	-597.90	-87.00	<1.4	<1.9	<2.4	/
268	14.789	1.099	-0.007	-0.019	<0.016	<0.020	-133.34	-331.37	<1.5	<1.8	<2.3	/
269	14.750	3.300	0.077	0.018	<-0.007	0.079	356.17	1045.77	<-0.2	2.4	<2.4	6.6
270	14.665	1.209	-0.010	-0.016	<0.010	<0.019	346.38	-1349.94	<0.8	<1.6	<1.8	/
271	14.499	1.273	-0.030	-0.009	<0.007	0.031	-377.18	-1576.57	<0.5	2.5	<2.5	-81.7
272	14.488	2.424	-0.002	-0.023	<0.008	0.023	-1043.39	-173.15	<0.3	1.0	<1.0	-47.5
273	13.538	2.024	-0.011	0.006	0.031	<0.013	-1142.40	440.06	1.5	<0.6	<1.6	/
274	13.457	10.834	-0.130	-0.054	-0.083	0.141	169.85	-567.88	-0.8	1.3	1.5	-78.7
275	13.270	3.837	0.013	0.105	<-0.019	0.106	831.83	416.70	<-0.5	2.8	<2.8	41.5
276	13.172	7.910	0.037	0.018	0.083	0.041	163.45	529.32	1.0	0.5	1.1	13.0
277	12.417	2.233	-0.070	-0.022	<0.009	0.073	-728.59	19.19	<0.4	3.3	<3.3	-81.3

Table 2. Stokes parameter flux densities and polarisation properties of the 1667 MHz maser spots.

No	Vel (km s^{-1})	I (Jy b^{-1})	Q (Jy b^{-1})	U (Jy b^{-1})	V (Jy b^{-1})	P (Jy b^{-1})	$\Delta\alpha$ (milli arcsec)	$\Delta\delta$ (milli arcsec)	m_c (%)	m_l (%)	m_t (%)	χ (°)
1	41.738	0.128	0.003	0.001	<0.001	<0.003	-408.58	1145.12	<0.8	<2.5	<2.6	/
2	41.578	0.058	0.001	0.002	<0.001	<0.002	-263.12	-292.51	<1.7	<3.9	<4.3	/
3	41.375	0.049	0.000	0.001	<0.002	<0.001	-445.48	-49.43	<4.1	<2.0	<4.6	/
4	41.289	0.066	0.000	-0.001	<-0.002	<0.001	-679.07	493.79	<-3.0	<1.5	<3.4	/
5	40.476	0.089	-0.001	0.004	<-0.004	<0.004	-1112.70	-114.53	<-4.5	<4.6	<6.4	/
6	40.257	0.105	-0.002	0.003	<0.003	<0.004	-798.36	1266.66	<2.9	<3.4	<4.5	/
7	39.946	0.092	0.003	0.001	<0.006	<0.003	-1300.72	-52.34	<6.5	<3.4	<7.3	/
8	39.741	0.333	-0.083	-0.021	<0.003	0.086	-641.05	1334.74	<0.9	25.7	25.7	8.0
9	39.710	0.412	-0.078	-0.039	<0.004	0.087	-813.44	1660.42	<1.0	21.2	21.2	14.2
10	39.591	0.072	-0.002	-0.003	<0.005	<0.004	1231.57	-42.21	<6.9	<5.0	<8.5	/
11	39.337	0.071	0.001	0.000	<-0.002	<0.001	-668.28	603.22	<-2.8	<1.4	<3.1	/
12	39.268	0.050	0.000	-0.001	<0.001	<0.001	-1890.48	563.72	<2.0	<2.0	<2.8	/
13	38.960	0.052	0.002	-0.001	<-0.001	<0.002	-1159.69	1550.24	<-1.9	<4.3	<4.7	/
14	38.811	0.095	0.001	-0.002	<0.003	<0.002	-710.26	1899.06	<3.2	<2.4	<4.0	/
15	38.375	0.061	0.002	-0.002	<0.003	<0.003	1064.87	-304.76	<4.9	<4.6	<6.7	/
16	38.071	0.047	0.000	-0.005	<-0.003	<0.005	-1237.82	1762.63	<-6.4	<10.6	<12.4	/
17	38.032	0.110	0.003	-0.002	<0.015	<0.004	-895.46	2232.10	<13.6	<3.3	<14.0	/
18	37.836	0.162	0.004	0.005	<0.003	<0.006	-579.23	1792.08	<1.9	<4.0	<4.4	/
19	37.646	0.154	0.002	0.008	<-0.006	<0.008	-761.38	2194.98	<3.9	<5.4	<6.7	/
20	37.547	0.039	0.000	-0.001	<0.002	<0.001	-1223.82	1373.09	<5.1	<2.6	<5.7	/
21	37.501	0.081	0.001	-0.003	<0.005	<0.003	1919.19	659.47	<6.2	<3.9	< 7.3	/
22	37.490	0.063	0.001	0.006	<-0.001	<0.006	2118.80	-833.79	<-1.6	<9.7	<9.8	/
23	37.081	0.063	0.001	0.002	<-0.003	<0.002	1564.55	-14.37	<-4.8	<3.5	<5.9	/
24	36.831	0.044	0.000	0.001	<-0.002	<0.001	-908.98	751.68	<-4.5	<2.3	<5.1	/
25	36.556	0.047	-0.001	-0.002	<-0.002	<0.002	1860.45	-368.92	<-4.3	<4.8	<6.4	/
26	35.959	0.050	-0.003	0.002	< 0.005	<0.004	-1348.83	-599.24	<10.0	<7.2	<12.3	/
27	35.885	0.045	-0.002	-0.002	<0.003	<0.003	-750.66	-1242.32	<6.7	<6.3	<9.2	/
28	35.759	0.056	0.002	0.002	<0.007	<0.003	1621.80	1194.01	<12.5	<5.1	<13.5	/
29	35.228	0.050	0.000	-0.002	<0.002	<0.002	1435.26	712.92	<4.0	<4.0	<5.7	/
30	34.335	0.046	-0.001	-0.001	<-0.004	<0.001	2324.59	-29.23	<-8.7	<3.1	<9.2	/
31	33.613	0.045	0.000	-0.002	<0.002	<0.002	1709.14	555.28	<4.4	<4.4	<6.2	/
32	33.608	0.046	0.000	0.002	<-0.004	<0.002	-436.95	-1268.20	<-8.7	<4.3	<9.7	/
33	33.395	0.045	-0.001	-0.002	<0.001	<0.002	-2024.91	-576.04	<2.2	<5.0	<5.5	/
34	33.385	0.054	-0.002	0.002	<0.005	<0.003	1244.43	1541.89	<9.3	<5.2	<10.7	/
35	33.102	0.048	-0.001	0.000	<0.003	<0.001	1475.83	1114.38	<6.2	<2.1	<6.5	/
36	32.925	0.045	-0.004	-0.002	<-0.001	<0.004	1751.05	1768.30	<-2.2	<9.9	<10.1	/
37	32.235	0.049	-0.001	-0.002	<-0.004	<0.002	-2232.85	-486.10	<-8.2	<4.6	<9.4	/
38	31.329	0.069	-0.002	0.002	<0.003	<0.003	1574.43	2239.40	<4.3	<4.1	<5.9	/
39	30.991	0.082	-0.001	0.002	<-0.002	<0.002	1840.89	1822.02	<-2.4	<2.7	<3.6	/
40	30.646	0.052	0.000	0.004	<0.001	<0.004	-1344.00	-1513.96	<1.9	<7.7	<7.9	/
41	30.511	0.033	0.000	0.001	<0.003	<0.001	2337.28	-366.99	<9.1	<3.0	<9.6	/
42	29.935	0.037	0.001	-0.001	<0.002	<0.001	2279.15	-73.57	<5.4	<3.8	<6.6	/
43	28.659	0.045	0.002	0.013	<-0.002	<0.013	-1640.66	-858.86	<-4.4	<29.2	<29.5	/
44	28.159	0.059	-0.003	0.003	<-0.002	<0.004	-1367.02	-1224.05	<-3.4	<7.2	<8.0	/
45	27.823	0.047	0.000	0.003	<-0.004	<0.003	-929.74	-1574.25	<-8.5	<6.4	<10.6	/
46	26.836	0.058	-0.001	0.001	<-0.001	<0.001	-1164.18	-1534.38	<-1.7	<2.4	<2.9	/
47	26.189	0.068	-0.004	0.002	<-0.002	<0.004	-1194.21	-1356.57	<-2.9	<6.6	<7.2	/
48	25.353	0.054	0.003	0.002	<-0.001	<0.004	-1245.32	-1154.12	<-1.9	<6.7	<7.0	/
49	24.934	0.053	-0.012	0.003	<-0.003	<0.012	-990.58	-1516.78	<-5.7	<23.3	<24.0	/
50	23.928	0.056	0.001	-0.003	<-0.002	<0.003	-888.89	-1711.43	<-3.6	<5.6	<6.7	/
51	22.335	0.066	-0.002	0.003	<0.003	<0.004	-983.61	-1472.53	<4.5	<5.5	<7.1	/
52	21.564	0.050	0.007	0.004	<0.003	<0.008	-587.55	-1160.84	<6.0	<16.1	<17.2	/
53	21.200	0.049	0.001	0.003	<0.002	<0.003	-313.81	-1555.92	<4.1	<6.5	<7.7	/
54	20.859	0.052	0.003	-0.001	<0.001	<0.003	-801.46	-1566.29	<1.9	<6.1	<6.4	/
55	20.807	0.068	-0.002	0.009	<-0.002	<0.009	-1250.28	-1090.17	<-2.9	<13.6	<13.9	/
56	20.129	0.066	-0.003	-0.003	<0.001	<0.004	-164.46	-1350.00	<1.5	<6.4	<6.6	/
57	20.062	0.045	0.001	-0.003	<0.004	<0.003	-419.49	-1057.55	<8.9	<7.0	<11.3	/
58	19.887	0.047	-0.001	0.002	<0.003	<0.002	-1027.02	-2031.79	<6.4	<4.8	<8.0	/
59	19.857	0.080	0.001	-0.001	<0.008	<0.001	-1054.94	-1113.25	<10.0	<1.8	<10.2	/
60	19.818	0.073	-0.001	-0.004	<0.002	<0.004	-585.24	-1633.24	<2.7	<5.6	<6.2	/
61	19.446	0.060	-0.002	-0.003	<0.005	<0.004	15.95	-1184.34	<8.3	<6.0	<10.2	/
62	18.786	0.048	0.000	0.002	<-0.002	<0.002	-928.26	2309.68	<-4.2	<4.2	<5.9	/
63	18.027	0.059	-0.002	-0.002	<-0.002	<0.003	-613.63	2332.24	<-3.4	<4.8	<5.9	/
64	17.971	0.096	0.002	0.002	<-0.002	<0.003	-519.49	-1063.93	<-2.1	<2.9	<3.6	/

Table 2. *continued*

No	Vel (km s^{-1})	I (Jy b^{-1})	Q (Jy b^{-1})	U (Jy b^{-1})	V (Jy b^{-1})	P (Jy b^{-1})	$\Delta\alpha$ (milli arcsec)	$\Delta\delta$ (milli arcsec)	m_c (%)	m_l (%)	m_t (%)	χ (°)
65	17.760	0.083	0.004	0.003	<0.006	<0.005	-831.41	-1816.88	<7.2	<6.0	<9.4	/
66	17.550	0.044	0.006	-0.007	<0.005	<0.009	-521.83	-1955.23	<11.4	<21.0	<23.9	/
67	16.585	0.068	0.000	0.001	<0.010	<0.001	-932.56	1659.17	<14.7	<1.5	<14.8	/
68	16.438	0.098	0.000	-0.001	<-0.005	<0.001	-175.36	-746.33	<-5.1	<1.0	<5.2	/
69	16.331	0.056	0.002	-0.002	<-0.018	<0.003	-1823.00	1254.70	<-32.1	<5.1	<32.5	/
70	16.051	0.113	-0.002	-0.010	<0.002	<0.010	-806.40	-753.89	<1.8	<9.0	<9.2	/
71	15.567	0.064	0.003	-0.004	<-0.001	<0.005	-1667.70	500.25	<-1.6	<7.8	<8.0	/
72	15.431	0.088	0.000	-0.003	<0.002	<0.003	-848.90	1789.53	<2.3	<3.4	<4.1	/
73	15.371	0.060	0.000	-0.001	<0.001	<0.001	-813.00	307.30	<1.7	<1.7	<2.4	/
74	15.201	0.081	0.001	-0.002	<0.002	<0.002	-2033.58	1751.19	<2.5	<2.8	<3.8	/
75	15.067	0.101	0.000	0.000	<0.002	0.000	-1557.10	913.63	<2.0	0.0	<2.0	/
76	15.047	0.128	0.006	-0.003	<0.002	<0.007	-212.33	-250.46	<1.6	<5.2	<5.4	/
77	14.513	0.046	-0.003	-0.002	<0.002	<0.004	-2195.43	67.66	<4.3	<7.8	<8.9	/
78	13.758	0.058	0.000	-0.002	<-0.006	<0.002	-706.63	-455.27	<-10.3	<3.4	<10.8	/
79	13.693	0.096	0.001	0.001	<-0.001	<0.001	551.41	-1170.30	<-1.0	<1.5	<1.8	/
80	13.192	0.082	0.004	0.003	<0.005	<0.005	-322.85	1701.39	<6.1	<6.1	<8.6	/
81	12.441	0.059	0.000	0.003	<-0.002	<0.003	460.17	1516.60	<-3.4	<5.1	<6.1	/

Table 3. Stokes parameter flux densities and polarisation properties of the 1665 MHz maser spots.

No	Vel (km s^{-1})	I (Jy b^{-1})	Q (Jy b^{-1})	U (Jy b^{-1})	V (Jy b^{-1})	P (Jy b^{-1})	$\Delta\alpha$ (milli arcsec)	$\Delta\delta$ (milli arcsec)	m_c (%)	m_l (%)	m_t (%)	χ ($°$)
1	41.31	0.088	0.007	0.005	0.023	<0.009	1215.12	280.05	26.1	<9.8	<27.9	/
2	41.22	0.068	0.006	-0.005	<0.008	<0.008	865.90	1498.96	<11.8	<11.5	<16.5	/
3	40.99	0.107	-0.002	0.006	<0.008	<0.006	-708.11	266.12	<7.5	<5.9	<9.5	/
4	40.85	0.055	0.003	0.007	<0.001	<0.008	-411.86	-239.71	<1.8	<13.8	<13.9	/
5	40.78	0.093	-0.008	-0.007	<0.013	<0.011	-218.68	-403.23	<14.0	<11.4	<18.1	/
6	40.66	0.109	-0.010	0.008	<-0.006	<0.013	-1240.89	743.75	<-5.5	<11.7	<12.9	/
7	40.35	0.091	-0.008	-0.015	<-0.018	<0.017	-1406.84	1042.45	<-19.8	<18.7	<27.2	/
8	40.24	0.085	0.010	-0.012	<-0.003	<0.016	-1926.92	1717.89	<-3.5	<18.4	<18.7	/
9	12.01	0.583	0.040	-0.034	<0.007	0.052	4.38	-17.37	<1.2	9.0	9.1	-20.2
10	11.87	0.420	0.030	-0.007	0.016	0.031	-22.98	114.11	3.8	7.3	8.2	-6.6